A mixed finite-element, finite-volume, semi-implicit discretisation for atmospheric dynamics:
Cartesian geometry

Thomas Melvin[a]*, Tommaso Benacchio[a], Ben Shipway[a], Nigel Wood[a], John Thuburn[b] and Colin Cotter[c]

[a]*Met Office, Exeter, U.K.*

[b]*University of Exeter, U.K.*

[c]*Imperial College, London, U.K.*

*Correspondence to: Thomas Melvin, Met Office, FitzRoy Road, Exeter EX1 3PB, U.K. E-mail: Thomas.Melvin@metoffice.gov.uk

To meet the challenges posed by future generations of massively parallel supercomputers a reformulation of the dynamical core for the Met Office's weather and climate model is presented. This new dynamical core uses explicit finite-volume type discretisations for the transport of scalar fields coupled with an iterated-implicit, mixed finite-element discretisation for all other terms. The target model aims to maintain the accuracy, stability and mimetic properties of the existing Met Office model independent of the chosen mesh while improving the conservation properties of the model. This paper details that proposed formulation and, as a first step towards complete testing, demonstrates its performance for a number of test cases in (the context of) a Cartesian domain. The new model is shown to produce similar results to both the existing semi-implicit semi-Lagrangian model used at the Met Office and other models in the literature on a range of bubble tests and orographically forced flows in two and three dimensions.

1. Introduction

The dynamical core of a weather and climate prediction model is responsible for simulating those fluid dynamical aspects that are resolved on the mesh that is chosen for the spatial discretisation. The governing fluid dynamical equations are well known and presented in section 2. The principal properties required of a dynamical core are the accuracy, numerical stability and efficiency with which those equations are numerically approximated (see, for example, Lauritzen *et al.* (2011) for a discussion of various such aspects). The current trend of supercomputer architectures is towards a greatly increasing number of processors, together with an increasingly complex hierarchy of heterogeneous processors and memories. In terms of the efficiency of a dynamical core this trend shifts interest from optimising the number of calculations towards optimising the management of memory and communications between processors, (Lawrence *et al.* 2017). This has led to a renewed interest in the choice of mesh used and in particular to a desire, for those still using it, to move away from a latitude-longitude mesh, (Staniforth and Thuburn 2012). However, as noted by Staniforth and Thuburn (2012) the latitude-longitude mesh confers a number of advantages over many of the alternative meshes. The challenge then is to use spatial discretisations that retain the same accuracy and stability on the alternative meshes as obtained with latitude-longitude meshes.

The mixed finite-element approach of Cotter and Shipton (2012); Cotter and Thuburn (2014); Thuburn and Cotter (2015) is attractive as it achieves numerical consistency without relying on the orthogonality of the mesh. Those authors focused on the shallow-water equations and developed a scheme that shares many of the beneficial properties of the C-grid finite-difference scheme, in particular good wave dispersion properties together with the necessary conditions to avoid spurious computational modes. This approach is very general in terms of the order of accuracy; arbitrarily high-order schemes can be straightforwardly defined. In line with most current dynamical cores, here only second-order accuracy for the non-transport aspects (i.e. those aspects principally responsible for wave propagation) is sought. Therefore the lowest-order version of the mixed finite-element scheme is used here but extended to the three dimensional Euler equations (see section 4). This is achieved by extending the hierarchy of finite-element spaces to include the particular temperature space proposed by Natale *et al.* (2016); Guerra and Ullrich (2016); Melvin *et al.* (2018). At lowest order this space resembles a finite-difference Charney-Phillips staggering of temperature. In particular it gives a finite-element scheme that has good wave dispersion properties for vertically propagating waves, as well as having the necessary conditions to avoid spurious computational modes in three dimensions.

A critical component of a weather and climate prediction system is the numerical scheme used for the transport of scalar quantities, e.g. the semi-Lagrangian scheme (Staniforth and Côté 1991) has proven to be a very effective scheme and is used by many operational weather and climate prediction centres. However, an important weakness of virtually all such schemes is that they do not conserve the quantity they transport. Here the aim is to retain the good properties of the semi-Lagrangian scheme, namely an upwind scheme with small dispersive errors and scale-selective damping and with flexibility in the order of the scheme, but to additionally provide a flux-form scheme, at least for the density field, and hence exact conservation. Since the lowest-order finite-element scheme is second-order, this means using a transport scheme that is separate from the rest of the dynamical core (as is the case generally for most models and in particular for semi-implicit semi-Lagrangian schemes). Whilst the transport scheme could be a finite-element scheme, here (following Thuburn and Cotter (2015)) a finite-volume scheme is used (presented in section 5) as that would seem a straightforward way of retaining the desired properties. Specifically a method of lines approach is used in which third-order upwind polynomial reconstructions are coupled with a third-order Runge-Kutta temporal discretisation.

The temporal discretisation scheme described here takes as its starting point the dynamical core described in Wood *et al.* (2014) (referred to there as the "standard SISL" version) which forms the basis of the weather and climate prediction system described by Walters *et al.* (2017) and Williams *et al.* (2015). In particular it is desired to retain the good temporal accuracy and long time step stability of that model. So while this work describes the replacement of the spatial discretisation and transport schemes of Wood *et al.*

(2014), the present scheme uses a similar iterated-implicit temporal discretisation, an overview of which is given in section 3 and a more detailed treatment in section 6. The current scheme differs from that of Wood *et al.* (2014) due to the presence, in the mixed finite-element method, of non-diagonal mass matrices, which complicates the solution of the implicit system of equations.

Although the development of this scheme is motivated by its application to non-orthogonal global meshes on the sphere, it is important that it has good accuracy on Cartesian meshes; without this its performance on the global meshes is unlikely to be acceptably good and it certainly will not be acceptable as the basis for regional modelling. Therefore, example computational results from a variety of essentially two-dimensional and also some three-dimensional test cases are reported in section 7 before a concluding discussion in section 8.

2. Continuous equations

The Euler equations for a perfect gas in a rotating frame are

$$\frac{\partial \mathbf{u}}{\partial t} = -\boldsymbol{\xi} \times \mathbf{u} - 2\boldsymbol{\Omega} \times \mathbf{u} - \nabla\left(K + \Phi\right) - c_p \theta \nabla \Pi,$$

(1)

$$\frac{\partial \rho}{\partial t} = -\nabla \cdot (\rho \mathbf{u}),$$

(2)

$$\frac{\partial \theta}{\partial t} = -\mathbf{u} \cdot \nabla \theta,$$

(3)

together with the nonlinear equation of state

$$\Pi^{\left(\frac{1-\kappa}{\kappa}\right)} = \frac{R}{p_0}\rho\theta,$$

(4)

where: $\mathbf{u}$ is the velocity vector; $\boldsymbol{\xi} \equiv \nabla \times \mathbf{u}$ is the relative vorticity; $\boldsymbol{\Omega}$ is the rotation vector; $K \equiv \frac{1}{2}\mathbf{u} \cdot \mathbf{u}$ is the kinetic energy per unit mass; Φ is the geopotential such that $\nabla\Phi = -\boldsymbol{g}$ where $\boldsymbol{g}$ is the acceleration due to gravity; c_p is the specific heat at constant pressure; θ is potential temperature, related to temperature through $T = \theta\Pi$; $\Pi = (p/p_0)^\kappa$ is the Exner pressure with p pressure and p_0 a constant reference pressure; R is the gas constant per unit mass; $\kappa \equiv R/c_p$; and ρ is density.

These equations are solved subject to the boundary condition of zero mass flux through the boundaries of the domain.

Note that following Cotter and Shipton (2012); Cotter and Thuburn (2014); Thuburn and Cotter (2015) the velocity equation is written in the vector-invariant form. In the shallow-water form of the equations this allows the discretised version of the equations to retain some of the mimetic properties discussed by Staniforth and Thuburn (2012). The scheme presented here targets most of the desirable criteria outlined in Staniforth and Thuburn (2012), but notably it does not target conservation of energy or axial angular momentum.

3. Overview of the spatio-temporal discretisation

The temporal discretisation of the equations is inspired by the iterative-semi-implicit semi-Lagrangian discretisation such as that used in Wood *et al.* (2014). In that scheme all advective terms are handled using a semi-Lagrangian scheme. In the implementation of Wood *et al.* (2014) the advected quantities are the start of timestep fields whilst, at convergence of the iterative scheme, the advecting velocity is averaged in time. All other terms are handled using an iterative-implicit temporal discretisation.

The same basic discretisation is targeted here but with the following differences:

1. To achieve good conservation properties, instead of a semi-Lagrangian scheme, an explicit Eulerian flux-form scheme is used for the continuity equation.

2. A similar scheme is also used for potential temperature but in advective form (this is to achieve good wave dispersion properties by avoiding the need to average the vertical wind).

3. The self-advection terms in the velocity equation (which in the vector invariant form of the equation are manifested in the kinetic energy ∇K and vorticity $\boldsymbol{\xi} \times \mathbf{u}$ terms of (1)) are averaged in time and evaluated iterative-implicitly.

4. A mixed finite-element spatial discretisation is used in place of the finite-difference one used in Wood *et al.* (2014).

First consider the velocity equation (1). This can be written as

$$\frac{\partial \mathbf{u}}{\partial t} = \mathbf{S}, \tag{5}$$

where

$$\mathbf{S} \equiv -\boldsymbol{\xi} \times \mathbf{u} - 2\boldsymbol{\Omega} \times \mathbf{u} - \nabla\left(K + \Phi\right) - c_p \theta \nabla \Pi. \tag{6}$$

This is first integrated in time to give

$$\frac{\mathbf{u}\left(\mathbf{x}, t + \Delta t\right) - \mathbf{u}\left(\mathbf{x}, t\right)}{\Delta t} = \frac{1}{\Delta t} \int_t^{t+\Delta t} \mathbf{S} dt, \tag{7}$$

where $\mathbf{x}$ is a fixed position. The right-hand side time integral is then approximated using a, possibly off-centred, trapezoidal rule to give

$$\delta_t \mathbf{u} = \overline{\mathbf{S}}^\alpha, \tag{8}$$

where, for a generic scalar or vector variable F,

$$\delta_t F \equiv \frac{F^{n+1} - F^n}{\Delta t}, \tag{9}$$

and

$$\overline{F}^\alpha \equiv \alpha F^{n+1} + (1 - \alpha) F^n. \tag{10}$$

The parameter α is an off-centring parameter which takes the value $1/2$ for a centred scheme. The superscripts $n + 1$ and n denote the time-level of a variable.

Using the same notation, the density equation (2) and potential temperature equation (3) are discretised as

$$\delta_t \rho = -\nabla \cdot \left[\boldsymbol{\mathcal{F}} \left(\rho^n, \overline{\mathbf{u}}^{1/2} \right) \right], \tag{11}$$

$$\delta_t \theta = -\mathcal{A} \left(\theta^n, \overline{\mathbf{u}}^{1/2} \right), \tag{12}$$

where $\overline{\mathbf{u}}^{1/2}$ indicates that the advecting velocity is a centred average in time, $\boldsymbol{\mathcal{F}} \left(\rho^n, \overline{\mathbf{u}}^{1/2} \right)$ is the time-averaged flux of density and $\mathcal{A} \left(\theta^n, \overline{\mathbf{u}}^{1/2} \right)$ is the time-averaged advection tendency of the potential temperature.

All terms are discretised in space using the mixed finite-element scheme described in section 4, except for $\mathcal{F}$ and $\mathcal{A}$ which are discretised using the finite-volume scheme described in section 5.

Eqs. (8)-(12) and (4) represent a set of coupled, non-linear equations. These are solved using a quasi-Newton method that is detailed in section 6.

104 **4. The mixed finite-element discretisation**

105 *4.1. Subdivision of domain*

106 The three-dimensional model domain (D, with boundary ∂D) is partitioned into a mesh consisting of a number of cells (C), each cell

107 having a number of faces (F), edges (E) and vertices (V). Where appropriate, subscripts D, C, F, E and V, respectively, will be used

108 to denote evaluation of quantities over objects of these types. Here, in three dimensions, hexahedral cells are used that are aligned in

109 columns in the vertical (with their lateral faces having normals that are perpendicular to gravity).

110 *4.2. Function spaces*

111 To form the finite-element function spaces in three dimensions the sequence of finite element spaces of Natale *et al.* (2016) is used.

112 This sequence is the natural extension of the two-dimensional function spaces used for the shallow water equations presented in Cotter

113 and Shipton (2012); Thuburn and Cotter (2015).

114 There are 4 principal function spaces, denoted by $\mathbb{W}_i$, $i = 0, 1, 2, 3$, each of which has specific attributes and, in particular, varying

115 degrees of continuity across cell boundaries. These spaces are related by the de Rham complex (Bott and Raoul 1982):

$$\mathbb{W}_0 \xrightarrow{\nabla} \mathbb{W}_1 \xrightarrow{\nabla\times} \mathbb{W}_2 \xrightarrow{\nabla\cdot} \mathbb{W}_3. \qquad (13)$$

116 These function spaces at order l for hexahedral elements correspond to:

117 $\mathbb{W}_0$ The Q_{l+1} space of scalar functions;

118 $\mathbb{W}_1$ The Nédélec N_l space of vector functions;

119 $\mathbb{W}_2$ The Raviart-Thomas RT_l space of vector functions;

120 $\mathbb{W}_3$ The Q_l^{DG} space of scalar functions.

121 Further details on these spaces can be found in Boffi *et al.* (2013). This de Rham complex is complemented by the additional function

122 spaces:

123 $\mathbb{W}_\theta$ The space of scalar functions based on the vertical part of $\mathbb{W}_2$; as discussed in Section 1 this is used to avoid vertical averaging

124 in the coupling between the vertical momentum and potential temperature equations and hence to obtain good numerical wave

125 dispersion properties;

126 $\mathbb{W}_\chi$ The Q_m^{DG} space of scalar functions, where m may be different from l; this allows the representation of the coordinate field to be

127 decoupled from the choice of the other finite element spaces.

128 Details on the structure of these spaces can be found in Appendix A. As noted in the Introduction, the choice of lowest-order

129 elements is made here, i.e. $l = 0$. Details of the form of the basis functions for this choice can be found in Appendix B.

130 *4.3. Variable expansions and weak forms*

131 Each variable is assigned to a function space that is consistent with its physical nature. Specifically: $\Phi \in \mathbb{W}_0$, pointwise scalar

132 functions; $\boldsymbol{\xi} \in \mathbb{W}_1$, vector functions corresponding to circulations; $\mathbf{u} \in \mathbb{W}_2$, vector functions corresponding to fluxes; and $\rho \in \mathbb{W}_3$,

133 scalar functions corresponding to volume integrals. Additionally, Π is placed in $\mathbb{W}_3$ and the form of the rotation vector $\boldsymbol{\Omega}$ is assumed

134 to be known analytically and so will be computed where needed. In order to obtain good wave dispersion properties equivalent to the

135 use of a Charney-Phillips grid and to avoid the computational mode of the Lorenz grid, $\theta \in \mathbb{W}_\theta$, see Melvin *et al.* (2018) for details on

136 this choice.

137 Each variable is expanded in the trial functions associated with its function space. Finally, the (time dependent) coefficients of this

138 expansion are chosen such that the projection of each equation onto test functions vanishes for all test functions from the appropriate

139 function space, i.e. the error is orthogonalised to the test function space. This is the discrete weak form of the equation.

140 For example, for a prototypical discrete equation, $f = 0$, for some variable f, the weak form of this equation is given by multiplying

141 the equation by a test function g and integrating over the domain

$$\int_D gf \, dV = 0, \tag{14}$$

142 and then requiring that this equation holds for all test functions g in the appropriate function space. Equation (14) can be concisely

143 written as

$$\langle g, f \rangle = 0. \tag{15}$$

144 The Galerkin method is followed in which the test functions are chosen from the same space as the trial functions. These functions

145 are given in appendix B. For each of $\mathbb{W}_0,...,\mathbb{W}_3$ these functions are usually denoted respectively by γ, $\mathbf{c}$, $\mathbf{v}$, and σ. The test function for

146 $\mathbb{W}_\theta$ is denoted by w.

147 Note that the boundary condition,

$$\mathbf{n}_{\partial D} \cdot \mathbf{u} = 0, \tag{16}$$

148 on the boundary of the domain, ∂D, (where $\mathbf{n}_{\partial D}$ is the outward normal to that boundary) is enforced in the expansion of the velocity,

149 $\mathbf{u}$, in the trial functions for $\mathbb{W}_2$. This boundary condition is only valid on the top and bottom of the domain, where it is appropriate to

150 apply a no flux boundary condition. For all the cases considered here (which use periodic boundary conditions in the horizontal), and

151 more generally for spherical domains, no extra boundary conditions are needed. However, for bounded domains (such as used for local

152 area modelling) extra flux integral boundary conditions would arise when integrating by parts (as done in the next section).

4.4. Weak form of the equations

4.4.1. Velocity equation

155 Using (6), multiplying (8) by test functions from $\mathbb{W}_2$ and integrating over the domain D gives the weak form of the velocity equation

156 as

$$\langle \mathbf{v}, \delta_t \mathbf{u} \rangle = -\overline{\langle \mathbf{v}, \boldsymbol{\xi} \times \mathbf{u} + 2\boldsymbol{\Omega} \times \mathbf{u} \rangle}^{\alpha}$$

$$-\overline{\langle \mathbf{v}, \nabla K + \nabla \Phi + c_p \theta \nabla \Pi \rangle}^{\alpha}, \tag{17}$$

157 However various quantities in this equation do not have the required continuity to permit the required vector operations to be evaluated.

158 • Exner pressure, Π, is discontinuous between cells, so $\nabla \Pi$ is not defined at cell boundaries. Additionally, the potential

159 temperature, θ, is only continuous between cells in the vertical direction. This prevents direct evaluation of (17). Instead, the

160 procedure is: first split the integration over the domain into the sum of integrations over cells; then integrate by parts over each

161 cell, introducing boundary integrals over the cell faces; and then rewrite as global integrals, i.e.

$$
\begin{aligned}
\langle \mathbf{v}, c_p \theta \nabla \Pi \rangle &= \sum_{\mathsf{C}} \langle c_p \theta \mathbf{v}, \nabla \Pi \rangle_{\mathsf{C}} \\
&= \sum_{\mathsf{F}} \langle\!\langle [\![c_p \theta \mathbf{v}]\!]_{\mathsf{F}}, \{\Pi\}_{\mathsf{F}} \rangle\!\rangle_{\mathsf{F}} \\
&\quad - \sum_{\mathsf{C}} \langle \nabla_{\mathsf{C}} \cdot (c_p \theta \mathbf{v}), \Pi \rangle_{\mathsf{C}} \\
&= \langle\!\langle [\![c_p \theta \mathbf{v}]\!], \{\Pi\} \rangle\!\rangle \\
&\quad - \langle \nabla_{\mathsf{C}} \cdot (c_p \theta \mathbf{v}), \Pi \rangle,
\end{aligned}
\tag{18}
$$

162 where: $\langle \cdot \rangle_{\mathsf{C}}$ indicates integration over a cell; $\nabla_{\mathsf{C}} \cdot$ indicates that the divergence is evaluated only within the interior of the cell,

163 excluding the faces; $\langle\!\langle \cdot \rangle\!\rangle_{\mathsf{F}}$ indicates integration over a face; and $\langle\!\langle \cdot \rangle\!\rangle$ indicates the sum of integrations over all faces (because

164 of the boundary condition (16) this sum is in fact only non-zero for interior faces). The notation $[\![\cdot]\!]_{\mathsf{F}}$ indicates the jump in its

165 argument across a face and $\{\cdot\}_{\mathsf{F}}$ indicates the value of its argument on a face, the choice made here is to use the average of the

166 discontinuous values on the face. The appearance of $[\![\cdot]\!]_{\mathsf{F}}$ and $\{\cdot\}_{\mathsf{F}}$ without subscripts indicates the sum of integrations over all

167 faces. For details of these operators see appendix C.

168 • Since $\mathbf{u} \in \mathbb{W}_2$, $\boldsymbol{\xi} = \nabla \times \mathbf{u}$ is not defined at cell boundaries. Therefore the vorticity $\boldsymbol{\xi} \in \mathbb{W}_1$ is obtained as the weak curl of $\mathbf{u}$ by

169 requiring that

$$
\langle \mathbf{c}, \boldsymbol{\xi} \rangle = \langle \nabla \times \mathbf{c}, \mathbf{u} \rangle - \langle\!\langle \mathbf{c}, \{\mathbf{u}\} \times \mathbf{n} \rangle\!\rangle,
\tag{19}
$$

170 for all $\mathbf{c} \in \mathbb{W}_1$ where $\mathbf{n}$ is the outward normal to each face. Note that, due to the uniqueness of $\{\mathbf{u}\}$ on faces, the boundary term,

171 $\langle\!\langle \cdot \rangle\!\rangle$, in (19) is only non-zero on the top and bottom boundaries of the domain. At these points, consistently with an assumed

172 free-slip condition on the velocity field, the value of $\{\mathbf{u}\}$ on the domain boundaries takes the value just inside the domain. This

173 choice results in the horizontal components of the vorticity being zero on the top and bottom boundaries of the domain.

174 • The kinetic energy, K, does not in general have any continuity between cells and its gradient is not defined. Therefore, this term

175 is integrated by parts to give

$$
\langle \mathbf{v}, \nabla K \rangle = - \langle \nabla \cdot \mathbf{v}, K \rangle,
\tag{20}
$$

176 where the boundary condition (16) has been used to eliminate the boundary integral.

177 Therefore, with the addition of a Rayleigh damping term, (17) becomes

$$
\begin{aligned}
\langle \mathbf{v}, \delta_t \mathbf{u} \rangle &= -\overline{\langle \mathbf{v}, \boldsymbol{\xi} \times \mathbf{u} \rangle}^{\alpha} - \overline{\langle \mathbf{v}, 2\boldsymbol{\Omega} \times \mathbf{u} \rangle}^{\alpha} \\
&\quad + \overline{\langle \nabla \cdot \mathbf{v}, K \rangle}^{\alpha} - \overline{\langle \mathbf{v}, \nabla \Phi \rangle}^{\alpha} \\
&\quad - \overline{\langle\!\langle [\![c_p \theta \mathbf{v}]\!], \{\Pi\} \rangle\!\rangle}^{\alpha} \\
&\quad + \overline{\langle \nabla_{\mathsf{C}} \cdot (c_p \theta \mathbf{v}), \Pi \rangle}^{\alpha} \\
&\quad - \overline{\left\langle \mathbf{v}, \mu \left(\frac{\mathbf{u} \cdot \mathbf{n}_b}{\mathbf{z}_b \cdot \mathbf{n}_b} \right) \mathbf{z}_b \right\rangle}^{1}.
\end{aligned}
\tag{21}
$$

178 For the Rayleigh damping term: μ is a damping profile that varies with height above the surface; the overbar $\overline{\langle\ \rangle}^{1}$ indicates that the

179 term is evaluated fully implicitly in time, i.e. at time level $n + 1$; $\mathbf{z}_b$ is the basis vector of $\mathbb{W}_2$ aligned with the vertical direction; and

180 $\mathbf{n}_b$ is the basis vector of $\mathbb{W}_1$ aligned with the direction normal to the vertically facing cell face (see Figure 1).
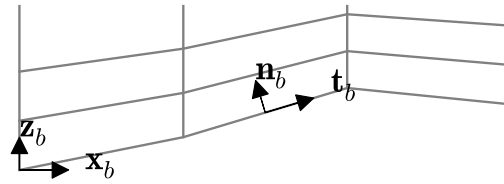
Figure 1. Unit vectors in terrain following coordinates, $\mathbf{z}_b$ is parallel to gravity and $\mathbf{x}_b$ is normal to gravity. $\mathbf{n}_b$ is normal to the model layers and $\mathbf{t}_b$ is parallel to model layers.

4.4.2. Continuity equation

Multiplying (11) by test functions from $\mathbb{W}_3$ and integrating over the domain D gives the weak form of the continuity equation as

$$\langle \sigma, \delta_t \rho \rangle = -\left\langle \sigma, \nabla \cdot \boldsymbol{\mathcal{F}}\left(\rho^n, \overline{\mathbf{u}}^{1/2}\right) \right\rangle, \tag{22}$$

where it is assumed that the transport scheme used to evaluate $\boldsymbol{\mathcal{F}}$ returns a vector in $\mathbb{W}_2$ so that its divergence is defined everywhere.

4.4.3. Thermodynamic equation

Multiplying (12) by test functions from $\mathbb{W}_\theta$ and integrating over the domain D gives the weak form of the thermodynamic equation as

$$\langle w, \delta_t \theta \rangle = -\left\langle w, \mathcal{A}\left(\theta^n, \overline{\mathbf{u}}^{1/2}\right) \right\rangle. \tag{23}$$

4.4.4. Equation of state

Multiplying (4) by test functions from $\mathbb{W}_3$ and integrating over the domain D gives the weak form of the equation of state as

$$\left\langle \sigma, \Pi^{\frac{1-\kappa}{\kappa}} \right\rangle = \left\langle \sigma, \frac{R}{p_0} \rho \theta \right\rangle. \tag{24}$$

4.5. Transformation to a reference cell

It is possible to evaluate the various integrals required for the weak formulation (i.e. (21), (22), (23) and (24)) directly in physical space. However, for any mesh other than one that consists of identical cells, this approach would require the evaluation of a number of integrals that are specific to each cell (for example the evaluation of the integral of the product of various basis functions). It is generally accepted that a more efficient approach is to transform the equations for each physical cell into a single, reference cell (Rognes *et al.* 2009). Then only one set of basis functions and one set of quadrature points are needed, rather than different sets being required for each cell.

Therefore, consider a mapping $\phi : \widehat{\mathsf{C}} \to \mathsf{C}$ between a reference cell $\widehat{\mathsf{C}}$ with coordinates $\widehat{\boldsymbol{\chi}} = (\widehat{\chi}_1, \widehat{\chi}_2, \widehat{\chi}_3)$ and a physical cell C with coordinates $\boldsymbol{\chi} = (\chi_1, \chi_2, \chi_3)$ such that $\boldsymbol{\chi} = \phi(\widehat{\boldsymbol{\chi}})$. Variables and operators in the reference cell are denoted with a $\widehat{}$ to differentiate them from the undressed variables and operators used to indicate evaluation in the physical cell.

It is important that the transformations between the physical and reference cells preserve the various geometric properties of the mixed finite-element discretisation. This would happen automatically if the metric tensor of the reference cell were the transformation of the metric tensor of the physical cell but this would reintroduce a dependency in the reference cell on the physical cell it is mapped with. Instead a Cartesian metric tensor is assumed for the reference cell independently of the physical cell. Therefore, preservation of the required properties is achieved by using a specific collection of transformations that are specific to each function space. These transformations are designed to preserve the hierarchy of the function spaces by preserving:

a) the appropriate continuity between cells, specifically maintaining continuity of vector components that are tangential to cell faces for vectors in $\mathbb{W}_1$ and vector components that are normal to cell faces for vectors in $\mathbb{W}_2$; and

b) the integrals appropriate to each space, i.e.: pointwise evaluation for $\mathbb{W}_0$, line integrals for $\mathbb{W}_1$, area integrals for $\mathbb{W}_2$, and volume integrals for $\mathbb{W}_3$.

The transformations will collectively be referred to as Piola transformations. They are given below for each of the function spaces. More details can be found in Rognes *et al.* (2009); Brezzi and Fortin (1991); Monk (2003). Furthermore, it is assumed that the physical space uses the same Cartesian metric tensor as the reference space.

- For scalar fields in $\mathbb{W}_0$, which represent pointwise scalars (0-forms), the transform is

$$\gamma\left(\boldsymbol{\chi}\right) \equiv \gamma\left[\boldsymbol{\phi}\left(\widehat{\boldsymbol{\chi}}\right)\right] = \widehat{\gamma}\left(\widehat{\boldsymbol{\chi}}\right), \tag{25}$$

which satisfies

$$\nabla\gamma = \mathbf{J}^{-T}\widehat{\nabla}\widehat{\gamma}, \tag{26}$$

where the Jacobian $\mathbf{J} \equiv \partial\boldsymbol{\phi}\left(\widehat{\boldsymbol{\chi}}\right)/\partial\widehat{\boldsymbol{\chi}}$ and $\mathbf{J}^{-T} \equiv \left(\mathbf{J}^{-1}\right)^{T}$.

- For vector fields in $\mathbb{W}_1$, which represent circulation vectors (1-forms), the covariant Piola transform is

$$\mathbf{c}\left(\boldsymbol{\chi}\right) \equiv \mathbf{c}\left[\boldsymbol{\phi}\left(\widehat{\boldsymbol{\chi}}\right)\right] = \mathbf{J}^{-T}\widehat{\mathbf{c}}\left(\widehat{\boldsymbol{\chi}}\right), \tag{27}$$

which satisfies

$$\nabla\times\mathbf{c}\left(\boldsymbol{\chi}\right) = \frac{\mathbf{J}}{\det\mathbf{J}}\widehat{\nabla}\times\widehat{\mathbf{c}}\left(\widehat{\boldsymbol{\chi}}\right). \tag{28}$$

- For vector fields in $\mathbb{W}_2$, which represent flux vectors (2-forms), the contravariant Piola transform is

$$\mathbf{v}\left(\boldsymbol{\chi}\right) \equiv \mathbf{v}\left[\boldsymbol{\phi}\left(\widehat{\boldsymbol{\chi}}\right)\right] = \frac{\mathbf{J}\widehat{\mathbf{v}}\left(\widehat{\boldsymbol{\chi}}\right)}{\det\mathbf{J}}, \tag{29}$$

which satisfies

$$\nabla\cdot\mathbf{v}\left(\boldsymbol{\chi}\right) = \frac{1}{\det\mathbf{J}}\widehat{\nabla}\cdot\widehat{\mathbf{v}}\left(\widehat{\boldsymbol{\chi}}\right). \tag{30}$$

- For scalars in $\mathbb{W}_3$, which represent volume averaged quantities (3-forms), the transformation would naturally be

$$\sigma\left(\boldsymbol{\chi}\right) \equiv \sigma\left[\boldsymbol{\phi}\left(\widehat{\boldsymbol{\chi}}\right)\right] = \frac{\widehat{\sigma}\left(\widehat{\boldsymbol{\chi}}\right)}{\det\mathbf{J}}. \tag{31}$$

Space	Function	Differential of Function
$\mathbb{W}_0$	$\gamma = \widehat{\gamma}$	
$\mathbb{W}_1$	$\mathbf{c} = \mathbf{J}^{-T}\widehat{\mathbf{c}}$	$\nabla\gamma = \mathbf{J}^{-T}\widehat{\nabla}\widehat{\gamma}$
$\mathbb{W}_2$	$\mathbf{v} = \mathbf{J}\widehat{\mathbf{v}}/\det\mathbf{J}$	$\nabla\times\mathbf{c} = \mathbf{J}\widehat{\nabla}\times\widehat{\mathbf{c}}/\det\mathbf{J}$
$\mathbb{W}_3$	$\sigma = \widehat{\sigma}$	$\nabla\cdot\mathbf{v} = \widehat{\nabla}\cdot\widehat{\mathbf{v}}/\det\mathbf{J}$

Table 1. Transformations between physical $\boldsymbol{\chi}$ and computational space $\widehat{\boldsymbol{\chi}}$, using the mapping $\boldsymbol{\phi}\left(\widehat{\boldsymbol{\chi}}\right) = \boldsymbol{\chi}$ and $\mathbf{J} \equiv \partial\boldsymbol{\phi}\left(\widehat{\boldsymbol{\chi}}\right)/\partial\widehat{\boldsymbol{\chi}}$.

However, use of (31) would result in the weak form of the divergence transforming as

$$\int_{\mathrm{D}} \sigma\nabla\cdot\mathbf{v}\,dV = \int_{\widehat{\mathrm{D}}} \frac{\widehat{\sigma}}{\det\mathbf{J}}\widehat{\nabla}\cdot\widehat{\mathbf{v}}\,d\widehat{V}, \tag{32}$$

where $d\widehat{V}$ denotes the transformation of the physical volume element, dV, and is given by $dV/\det\mathbf{J}$. For non-affine cells (which in the context of the present hexahedral cells means cells that are not parallelepipeds) $\det\mathbf{J}$ is not constant within a cell and therefore (32) cannot be integrated exactly using numerical integration, in fact it cannot even accurately represent a constant, so it is not even 1$^{\text{st}}$ order accurate. The solution applied here is rehabilitation (Bochev and Ridzal 2010) in which the $\mathbb{W}_3$ mapping (31) is modified to

$$\sigma\left(\boldsymbol{\chi}\right) \equiv \sigma\left[\boldsymbol{\phi}\left(\widehat{\boldsymbol{\chi}}\right)\right] = \widehat{\sigma}\left(\widehat{\boldsymbol{\chi}}\right). \tag{33}$$

Eq. (32) now becomes

$$\int_{\mathrm{D}} \sigma\nabla\cdot\mathbf{v}\,dV = \int_{\widehat{\mathrm{D}}} \widehat{\sigma}\widehat{\nabla}\cdot\widehat{\mathbf{v}}\,d\widehat{V}. \tag{34}$$

The rehabilitation method is designed so that the order of accuracy of the scheme is maintained on arbitrary meshes. This though comes at the expense that the divergence operator applied to a vector field in $\mathbb{W}_2$ no longer maps to $\mathbb{W}_3$. However, Natale *et al.* (2016) showed that for the kind of meshes looked at here (terrain-following in a Cartesian domain) the coordinate mapping is close enough to affine that both the rehabilitated and non-rehabilitated method have similar accuracy. Therefore, the loss of the property that the divergence of a vector field in $\mathbb{W}_2$ maps into $\mathbb{W}_3$ is not expected to impact the properties of the scheme.

Table 1 summarises the spaces and transformations for functions in each space $\mathbb{W}_0$ to $\mathbb{W}_3$. The additional function spaces $\mathbb{W}_\theta$ and $\mathbb{W}_\chi$ use the same transformations as $\mathbb{W}_0$ (i.e. those appropriate for pointwise scalars).

Additionally, (14) and (15) become

$$\int_{\widehat{\mathrm{D}}} gf\det\mathbf{J}\,d\widehat{V} \equiv \langle g, f\det\mathbf{J}\rangle, \tag{35}$$

where the angle bracket notation still denotes the domain volume integral but now with respect to the reference cell coordinates.

4.6. Discrete equations using the reference cell

Applying the coordinate transformations to (21) gives:

$$
\begin{aligned}
\left\langle \mathbf{J}\widehat{\mathbf{v}}, \frac{\mathbf{J}\delta_t\widehat{\mathbf{u}}}{\det \mathbf{J}} \right\rangle \;=\;& -\overline{\left\langle \mathbf{J}\widehat{\mathbf{v}}, \left(\mathbf{J}^{-T}\widehat{\boldsymbol{\xi}}\right) \times \left(\frac{\mathbf{J}\widehat{\mathbf{u}}}{\det \mathbf{J}}\right) \right\rangle}^{\alpha} \\
& -\overline{\left\langle \mathbf{J}\widehat{\mathbf{v}}, 2\boldsymbol{\Omega} \times \frac{\mathbf{J}\widehat{\mathbf{u}}}{\det \mathbf{J}} \right\rangle}^{\alpha} \\
& +\overline{\left\langle \widehat{\nabla}\cdot\widehat{\mathbf{v}}, \frac{1}{2}\left(\frac{\mathbf{J}\widehat{\mathbf{u}}}{\det \mathbf{J}}\right)\cdot\left(\frac{\mathbf{J}\widehat{\mathbf{u}}}{\det \mathbf{J}}\right) \right\rangle}^{\alpha} \\
& -\overline{\left\langle \widehat{\mathbf{v}}, \widehat{\nabla}\widehat{\Phi} \right\rangle}^{\alpha} \\
& -\overline{\left\langle\!\!\left\langle [\![c_p\widehat{\theta}\widehat{\mathbf{v}}]\!], \left\{\widehat{\Pi}\right\} \right\rangle\!\!\right\rangle}^{\alpha} \\
& +\overline{\left\langle c_p\widehat{\theta}\widehat{\nabla}_{\mathsf{C}}\cdot\widehat{\mathbf{v}} + \widehat{\mathbf{v}}\cdot\widehat{\nabla}_{\mathsf{C}}\left(c_p\widehat{\theta}\right), \widehat{\Pi} \right\rangle}^{\alpha} \\
& -\overline{\left\langle \mathbf{J}\widehat{\mathbf{v}}, \mu\left(\frac{\widehat{\mathbf{u}}\cdot\widehat{\mathbf{n}}_b}{\widehat{\mathbf{z}}_b\cdot\widehat{\mathbf{n}}_b}\right)\frac{\mathbf{J}\widehat{\mathbf{z}}_b}{\det \mathbf{J}} \right\rangle}^{1} ,
\end{aligned}
\tag{36}
$$

where $\langle\!\langle \cdot \rangle\!\rangle$ now denotes the surface integrals over the collection of all cell faces evaluated in the reference space and $[\![\cdot]\!]$ is defined in terms of normal vectors evaluated in the reference space. Also, the fact that the $\mathbb{W}_2$ contravariant Piola transformation (29) preserves surface integrals over cell faces has been used.

The vorticity $\widehat{\boldsymbol{\xi}}$ is obtained by evaluating

$$
\begin{aligned}
\left\langle \mathbf{J}^{-T}\widehat{\mathbf{c}}, \mathbf{J}^{-T}\widehat{\boldsymbol{\xi}}\det \mathbf{J} \right\rangle \;=\;& \left\langle \mathbf{J}\widehat{\nabla}\times\widehat{\mathbf{c}}, \frac{\mathbf{J}\widehat{\mathbf{u}}}{\det \mathbf{J}} \right\rangle \\
& -\left\langle\!\!\left\langle \mathbf{J}^{-T}\widehat{\mathbf{c}}, \mathbf{J}\left\{\widehat{\mathbf{u}}\right\}\times\mathbf{J}^{-T}\widehat{\mathbf{n}} \right\rangle\!\!\right\rangle .
\end{aligned}
\tag{37}
$$

For (22) the coordinate transformation gives:

$$
\langle \widehat{\sigma}, \det \mathbf{J}\delta_t\widehat{\rho} \rangle = -\left\langle \widehat{\sigma}, \widehat{\nabla}\cdot\widehat{\boldsymbol{\mathcal{F}}}\left(\widehat{\rho}^{\,n}, \overline{\widehat{\mathbf{u}}}^{1/2}\right) \right\rangle ,
\tag{38}
$$

where the fact that the transport scheme gives a flux that is in $\mathbb{W}_2$ has been used.

For (23) it gives:

$$
\left\langle \widehat{w}, \det \mathbf{J}\delta_t\widehat{\theta} \right\rangle = -\left\langle \widehat{w}, \det \mathbf{J}\widehat{\mathcal{A}}\left(\widehat{\theta}^{\,n}, \overline{\widehat{\mathbf{u}}}^{1/2}\right) \right\rangle .
\tag{39}
$$

Here $\widehat{\mathcal{A}}$ is constructed to be in the $\mathbb{W}_\theta$ reference space (see section 5.3.2) and is defined continuously as the transformation of $\mathcal{A} \equiv \mathbf{u}\cdot\nabla\theta$, i.e.

$$
\widehat{\mathcal{A}} = \frac{1}{\det \mathbf{J}}\widehat{\mathbf{u}}\cdot\widehat{\nabla}\widehat{\theta}.
\tag{40}
$$

And for (24) it gives:

$$
\left\langle \widehat{\sigma}, \det \mathbf{J}\widehat{\Pi}^{\frac{1-\kappa}{\kappa}} \right\rangle \;=\; \left\langle \widehat{\sigma}, \det \mathbf{J}\frac{R}{p_0}\widehat{\rho}\widehat{\theta} \right\rangle .
\tag{41}
$$

Solutions are sought such that these equations hold for all the test functions. To achieve this, as discussed in section 4.3, each of the prognostic variables is expanded as the product of temporally varying degrees of freedom with the spatially varying set of trial

functions. Thus:

$$\widehat{\mathbf{u}} = \sum_j \widetilde{u}_j\left(t\right) \widehat{\mathbf{v}}_j\left(\widehat{\boldsymbol{\chi}}\right), \tag{42}$$

$$\widehat{\rho} = \sum_j \widetilde{\rho}_j\left(t\right) \widehat{\sigma}_j\left(\widehat{\boldsymbol{\chi}}\right), \tag{43}$$

$$\widehat{\theta} = \sum_j \widetilde{\theta}_j\left(t\right) \widehat{w}_j\left(\widehat{\boldsymbol{\chi}}\right), \tag{44}$$

$$\widehat{\Pi} = \sum_j \widetilde{\Pi}_j\left(t\right) \widehat{\sigma}_j\left(\widehat{\boldsymbol{\chi}}\right), \tag{45}$$

where the sum is over all the trial functions of the appropriate space, and each of $\widetilde{u}_j$, $\widetilde{\rho}_j$, $\widetilde{\theta}_j$ and $\widetilde{\Pi}_j$ represents a vector of the degrees of freedom associated with the respective trial function $\widehat{\mathbf{v}}_j$, $\widehat{\sigma}_j$, $\widehat{w}_j$ and $\widehat{\sigma}_j$ (see appendix B for details).

Let $\widetilde{u}$ denote the vector made up of all the coefficients $\widetilde{u}_j$, i.e. $\widetilde{u} = \left[\widetilde{u}_1^T, \widetilde{u}_2^T, ...\right]^T$, and similarly for $\widetilde{\rho}$, $\widetilde{\theta}$, and $\widetilde{\Pi}$. Substituting the expansions (42)-(45) into (36), (38), and (39) leads to

$$M_2 \delta_t \widetilde{u} + M_\mu \overline{\widetilde{u}}^1 = \overline{R_{\mathbf{u}}}^\alpha, \tag{46}$$

$$M_3 \delta_t \widetilde{\rho} = R_\rho^F, \tag{47}$$

$$M_\theta \delta_t \widetilde{\theta} = R_\theta^A, \tag{48}$$

where, with the exception of the damping layer term in the momentum equation, $\overline{R_{\mathbf{u}}}^\alpha$, R_ρ^F and R_θ^A are defined to be the vectors obtained from the right-hand sides respectively of (36), (38), and (39), and the components of the mass matrices are defined as

$$\left(M_2\right)_{ij} \equiv \left\langle \mathbf{J}\widehat{\mathbf{v}}_i, \frac{\mathbf{J}\widehat{\mathbf{v}}_j}{\det \mathbf{J}} \right\rangle, \tag{49}$$

$$\left(M_3\right)_{ij} \equiv \left\langle \widehat{\sigma}_i, \det \mathbf{J}\widehat{\sigma}_j \right\rangle, \tag{50}$$

$$\left(M_\theta\right)_{ij} \equiv \left\langle \widehat{w}_i, \det \mathbf{J}\widehat{w}_j \right\rangle, \tag{51}$$

and

$$\left(M_\mu\right)_{ij} \equiv \left\langle \mathbf{J}\widehat{\mathbf{v}}_i, \mu\left(\frac{\widehat{\mathbf{v}}_j \cdot \widehat{\mathbf{n}}_b}{\widehat{\mathbf{z}}_b \cdot \widehat{\mathbf{n}}_b}\right) \frac{\mathbf{J}\widehat{\mathbf{z}}_b}{\det \mathbf{J}} \right\rangle. \tag{52}$$

4.7. *Calculation of the Jacobian*

For various calculations the Jacobian of the coordinate transformation from the reference cell to each physical cell, along with its determinant is required. This is achieved by setting $\boldsymbol{\phi}\left(\widehat{\boldsymbol{\chi}}\right) = \left[\phi_1\left(\widehat{\boldsymbol{\chi}}\right), \phi_2\left(\widehat{\boldsymbol{\chi}}\right), \phi_3\left(\widehat{\boldsymbol{\chi}}\right)\right]$ and placing each ϕ_i in $\mathbb{W}_\chi$, for $i = 1, 2, 3$. In the interior of the computational domain the coordinates are continuous fields. However, in a bi-periodic domain the coordinates are discontinuous across the computational "edges" of the domain where they jump by the length of the domain. Therefore $\mathbb{W}_\chi$ is chosen to be a discontinuous version of $\mathbb{W}_0$ (but for which the interior degrees of freedom are in fact continuous). The Jacobian can then be calculated everywhere it is needed and in particular it will have the appropriate values across the computational "edges" of a bi-periodic domain. See Appendix D for details of the computation of the Jacobian.

273   *4.8. Quadrature*

274   In order to numerically evaluate the various spatial integrals that are required, Gaussian quadrature is used with quadrature weights

275   denoted by λ_i and quadrature points denoted by $\widehat{\chi}_i$. Therefore, integrals of the form (35) are approximated by

$$\int_{\widehat{\mathsf{D}}} gf \det \mathbf{J}\, d\widehat{V} \approx \sum_{i=1}^{n} \lambda_i g\left(\widehat{\chi}_i\right) f\left(\widehat{\chi}_i\right) \det \mathbf{J}\left(\widehat{\chi}_i\right), \tag{53}$$

276   where the volume element has been absorbed into the quadrature weights, and n denotes the total number of quadrature points. Since

277   $\det \mathbf{J}$ is polynomial (see appendix D), if both g and f are also polynomial then, provided a suitable quadrature rule with enough

278   quadrature points is used, (53) is exact. For the lowest-order ($l = 0$) elements used here a 3-point Gaussian quadrature rule is used

279   in each direction. This is exact up to 5th-order polynomials and is chosen to ensure that, provided $\det \mathbf{J}$ is constant, then all terms

280   are integrated exactly. However, in the presence of orography $\det \mathbf{J}$ is a non-constant polynomial (see appendix D). Since in general

281   g and f may be such that the integrand contains factors proportional to $(\det \mathbf{J})^{-1}$ the approximation to the integral will not then be

282   exact. Results (not shown) using a 5-point Gaussian quadrature are visually indistinguishable from those presented using a 3-point rule,

283   indicating that the errors due to inexact quadrature are indeed small.

284   **5.   Finite-volume transport discretisation**

285   *5.1. Method of lines advection*

286   To complete the discretisation, expressions for mass flux $\widehat{\mathcal{F}}$ and the advection of potential temperature $\widehat{\mathcal{A}}$ are required. A method-

287   of-lines approach is used in which the temporal and spatial aspects are treated separately. The temporal aspects are handled using

288   an explicit Runge-Kutta scheme described in section 5.2 while the spatial aspects are handled by finite-volume upwind polynomial

289   reconstruction described in section 5.3.

290   The first step is to map from the finite-element degrees of freedom to finite-volume degrees of freedom. For the finite-volume

291   degrees of freedom, a C-grid staggering in the horizontal and a Charney-Phillips staggering in the vertical is chosen. A consequence

292   then of using the lowest-order mixed finite-element spaces described here is that there is a one-to-one correspondence between the

293   finite-volume and finite-element degrees of freedom and the mapping between them is trivial.

294   Although the advecting velocity $\overline{\mathbf{u}}^{1/2}$ is updated as part of the overall scheme, it is not updated within the transport scheme itself.

295   *5.2. Temporal aspects*

296   Consistent with using a finite-volume approach $\widehat{\mathcal{F}}$ and $\widehat{\mathcal{A}}$ are approximations to their average value over a time step. Let the pair

297   of generic variables y and f denote either the pair $\widehat{\rho}$ and $\widehat{\nabla} \cdot \widehat{\mathcal{F}}$, or the pair $\widehat{\theta}$ and $\widehat{\mathcal{A}}$. Then, to evaluate the time-averaged value of f,

298   denoted by $\overline{f}$, the equation

$$\frac{\partial y}{\partial t} = f, \tag{54}$$

299   is solved using an explicit Runge-Kutta scheme and $\overline{f}$ is obtained as the weighted sum of values used in the final stage of that scheme.

300   Therefore, if the m-stage Runge-Kutta scheme is written in terms of some known coefficients a_{ij} and b_k as

$$y^{(i)} = y^n + \Delta t \sum_{j=1}^{i-1} a_{ij} f\left(y^{(j)}\right), \quad i = 1, ..., m, \tag{55}$$

301

$$y^{n+1} = y^n + \Delta t \sum_{k=1}^{m} b_k f\left(y^{(k)}\right), \tag{56}$$

then $\overline{f}$ is given by

$$\overline{f} \equiv \sum_{k=1}^{m} b_k f\left(y^{(k)}\right).$$ (57)

Note that for the case of $f = \widehat{\nabla} \cdot \widehat{\mathcal{F}}$ the divergence operator used in this calculation is the same as that used in the finite-element scheme.

The specific Runge-Kutta scheme used here is the 3rd-order, 3-stage, strong stability preserving Runge-Kutta scheme (Gottlieb 2005).

5.3. *Spatial aspects*

All calculations are performed using the reference cell and its neighbours together with the specification of a uniform mesh.

5.3.1. *Mass flux*

The mass flux $\widehat{\mathcal{F}}$ on a cell face is evaluated as the product of the normal component of velocity on that face with an estimation of the density on that face. The normal velocity is obtained directly as the appropriate degree of freedom of the finite-element velocity field $\widehat{\mathbf{u}}$. The value of density on the face is obtained by: first constructing a one-dimensional polynomial representation of the density field as a function of the reference coordinate in the direction normal to the cell face; and then evaluating the polynomial at the cell face.

The polynomial, of even order p, is constructed using a stencil of $p+1$ cells. Noting that $p+1$ is odd, this stencil is centred about the cell that is immediately upwind of the target face. The coefficients of the polynomial are obtained by requiring that the volume integral of the polynomial over any cell in the stencil is equal to the mass in that cell. Specifically, the polynomial in powers of $\widehat{\chi}$ is given by

$$\widetilde{\rho}\left(\widehat{\chi}\right) = \sum_{i=0}^{p} a_i \widehat{\chi}^{\, i},$$ (58)

with the constraint

$$\int_{\widehat{\mathsf{C}}} \widetilde{\rho} d\widehat{V} = \int_{\widehat{\mathsf{C}}} \widehat{\rho}_i d\widehat{V} \equiv \widehat{\rho}_i,$$ (59)

over all cells i in the stencil. Here $\widehat{\rho}_i$ is the value of the density field in cell i, and the fact that the volume of the reference cell is chosen to be 1 has been used. From (58) the reconstructed value of $\widetilde{\rho}$ at the flux point $\widehat{\chi}_F$ can be obtained as

$$\widetilde{\rho}\left(\widehat{\chi}_F\right) = \sum_{i=0}^{p} \alpha_i \widehat{\rho}_i,$$ (60)

where the new coefficients α_i are linear combinations of the a_i and also depend upon $\widehat{\chi}_F$. Near the vertical boundaries of the domain, where there are not enough points to construct the polynomial, the order is reduced. This is done in steps of two in order to retain an upwind bias.

5.3.2. *Potential temperature advection*

To compute $\widehat{\mathcal{A}}$ a similar method to that for the mass flux is used in that it uses a one-dimensional polynomial reconstruction but of odd order p. However, in this case the polynomial is obtained by matching directly the values of the degrees of freedom of $\widehat{\theta}$ in an appropriate stencil. The stencil has an even number $p+1$ of points and is biased in the upwind direction. The gradient of $\widehat{\theta}$ is obtained by differentiating the polynomial and evaluating the derivative at the position of the desired degree of freedom of $\widehat{\theta}$. This derivative is multiplied by the evaluation of $\widehat{\mathbf{u}}$ at that point (where $\{\widehat{\mathbf{u}}\}$ is used where $\widehat{\mathbf{u}}$ is discontinuous).

330   The process is repeated for each of the three directions to provide a full three-dimensional update. Finally, this update is divided by

331     $\det \mathbf{J}$ to obtain $\widehat{\mathcal{A}}$ as defined by (40).

332   *5.3.3. Consistent metrics*

333   As identified by Klemp *et al.* (2003) in order to obtain accurate solutions for stratified flow over fine scale orography a consistent

334   discretisation of certain metric terms that arise due to the terrain following vertical coordinate is needed.

335   Consider a domain with terrain following coordinates as set out in Figure 1, where orthogonal physical unit vectors $\mathbf{x}_b$ and $\mathbf{z}_b$ are

336   normal and parallel to gravity and orthogonal terrain following unit vectors $\mathbf{t}_b$ and $\mathbf{n}_b$ are parallel and normal to the model levels. The

337   evolution of a scalar quantity q that is preserved over Lagrangian trajectories in this two-dimensional domain is governed by

$$\frac{\partial q}{\partial t} = -\dot{X}\frac{\partial q}{\partial X} - \dot{Z}\frac{\partial q}{\partial Z}, \tag{61}$$

338   where X is aligned with $\mathbf{x}_b$, $\dot{X}$ denotes the material derivative of X, Z is aligned with $\mathbf{z}_b$, and $\dot{Z}$ denotes the material derivative of Z.

339   If q is vertically stratified ($q = q(Z)$) and the flow is horizontal ($\dot{Z} \equiv 0$) then $\partial q/\partial t = 0$.

340   Consider now what is required for this result to hold in terrain-following coordinates (ζ, η) where ζ is aligned with $\mathbf{t}_b$ and η with

341     $\mathbf{n}_b$. In these coordinates

$$\frac{\partial q}{\partial t} = -\dot{\zeta}\frac{\partial q}{\partial \zeta} - \dot{\eta}\frac{\partial q}{\partial \eta}. \tag{62}$$

342   By inverting the transformation from (ζ, η) to (X, Z), it is found that

$$\dot{\zeta} = \frac{1}{J}\left(\frac{\partial Z}{\partial \eta}\dot{X} - \frac{\partial X}{\partial \eta}\dot{Z}\right), \tag{63}$$

$$\dot{\eta} = \frac{1}{J}\left(-\frac{\partial Z}{\partial \zeta}\dot{X} + \frac{\partial X}{\partial \zeta}\dot{Z}\right), \tag{64}$$

343   where J is the Jacobian of the coordinate transformation. Substituting these into (62) gives

$$\begin{aligned} \frac{\partial q}{\partial t} &= -\frac{1}{J}\left(\dot{X}\frac{\partial Z}{\partial \eta} - \dot{Z}\frac{\partial X}{\partial \eta}\right)\frac{\partial q}{\partial \zeta} \\ &\quad -\frac{1}{J}\left(-\dot{X}\frac{\partial Z}{\partial \zeta} + \dot{Z}\frac{\partial X}{\partial \zeta}\right)\frac{\partial q}{\partial \eta}. \end{aligned} \tag{65}$$

344   Therefore, for q to remain constant in time when $\dot{Z} = 0$ and $q = q(Z)$ it is required that

$$-\dot{X}\frac{1}{J}\frac{dq}{dZ}\left(\frac{\partial Z}{\partial \eta}\left.\frac{\partial Z}{\partial \zeta}\right|_A - \frac{\partial Z}{\partial \zeta}\left.\frac{\partial Z}{\partial \eta}\right|_A\right) = 0, \tag{66}$$

345   where the subscript A indicates terms computed by the advection operator. For the terrain following coordinate transformations used

346   here, the dominant term is $\partial Z/\partial \zeta$ and hence the term $\partial Z/\partial \zeta|_A$ computed by the advection operator along model layers needs to match

347   the metric term $\partial Z/\partial \zeta$ contained in the advecting velocity $\dot{\eta}$ normal to model layers.

348   As in Melvin *et al.* (2010) this is achieved by modifying (64) such that the $\partial Z/\partial \zeta$ term is computed by the advection operator. In

349   practice this is achieved by modifying the velocity vector used in the advection scheme according to

$$\widehat{u}_i^* = \widehat{u}_i + \widehat{\mathbf{u}} \cdot \widehat{\nabla}\chi_i - \widehat{\mathcal{A}}\left(\chi_i, \widehat{\mathbf{u}}\right)\det\left(\mathbf{J}\right), \quad i = 1, 2, 3, \tag{67}$$

where $\widehat{u}_i$ is the ith component of $\widehat{\mathbf{u}}$ and $\widehat{\mathcal{A}}(\chi_i, \widehat{\mathbf{u}})$ is the advection operator applied to the ith component of the coordinate field $\boldsymbol{\chi}$. This modification means that the metric term $\left(\widehat{\nabla}\chi_i\right)$ component of $\widehat{u}_i$, as computed by the finite element scheme, is replaced by that computed by the high-order upwind scheme $\widehat{\mathcal{A}}(\chi_i, \cdot)$. This then means that both the metric term components and the advected components of χ are computed using the same scheme and so there is no inconsistency. Although in principle this modification can be applied to the velocity vector for all advection terms, in order to remove the distortion over fine scale orography it is only necessary to apply it to the potential temperature advection term, such that $\overline{\widetilde{\mathbf{u}^*}}^{1/2}$ is used to advect $\widehat{\theta}^n$ in (40). Furthermore, for all the examples presented here a uniform mesh in the χ_1 and χ_2 directions is used such that (67) only results in modifying the vertical component of the velocity $\widehat{u}_3$.

6. Solution procedure

6.1. Notation

The convention followed below is that calligraphic $\mathcal{R}$'s indicate residuals of the equations to be solved. Gothic $\mathfrak{R}$'s denote linear combinations of these residuals. The italic R's of section (4.4) indicate right-hand sides of the equations.

6.2. Overview

The governing equations (46), (47), (48), and (41), can be compactly written as

$$\mathcal{R}\left(\mathbf{x}^{n+1}\right) = 0, \tag{68}$$

where $\mathbf{x}^{n+1} \equiv \left[\widehat{\mathbf{u}}^{n+1}, \widehat{\rho}^{n+1}, \widehat{\theta}^{n+1}, \widehat{\Pi}^{n+1}\right]^T$ is the sought after state vector at the next time step. A full Newton method would solve this equation iteratively as

$$\mathcal{J}\left(\mathbf{x}^{(k)}\right)\mathbf{x}' = -\mathcal{R}\left(\mathbf{x}^{(k)}\right), \tag{69}$$

where $\mathbf{x}' \equiv \mathbf{x}^{(k+1)} - \mathbf{x}^{(k)}$ is the increment to the state vector, $\mathcal{J}$ is the Jacobian of $\mathcal{R}$ with respect to $\mathbf{x}$, and superscript (k) indicates the iteration index of the Newton loop. However, $\mathcal{J}$ is a large matrix and its inverse is dense, therefore a quasi-Newton method is used in which the Jacobian is approximated by a simpler linear system

$$\mathcal{J}\left(\mathbf{x}^{(k)}\right)\mathbf{x}' \approx \mathcal{L}\mathbf{x}'. \tag{70}$$

Note that since both $\mathcal{J}$ and $\mathcal{L}$ operate on increments to the solution, at convergence of the iterative solution, the same full, nonlinear equations (68) are solved. The choice of whether or how to approximate $\mathcal{J}$ affects whether, and how quickly, the iterative scheme convergences and also the computational efficiency of the scheme.

Following the approach of Wood *et al.* (2014), the choice of the linear operator $\mathcal{L}$ is inspired by the linearisation of $\mathcal{R}$ about some reference state $\mathbf{x}^*$ to obtain $\mathcal{L}(\mathbf{x}^*)$ and then solve

$$\mathcal{L}(\mathbf{x}^*)\mathbf{x}' = -\mathcal{R}\left(\mathbf{x}^{(k)}\right). \tag{71}$$

The spatially continuous form of $\mathcal{L}$ in physical space is given by

$$
\mathcal{L}\left(\mathbf{x}^*_{\mathrm{phys}}\right)\mathbf{x}'_{\mathrm{phys}} =
\begin{cases}
\mathbf{u}' - \mu\left(\frac{\mathbf{n}_b\cdot\mathbf{u}'}{\mathbf{n}_b\cdot\mathbf{z}_b}\right)\mathbf{z}_b \\[2mm]
\quad + \tau_u\Delta t c_p\left(\theta'\nabla\Pi^* + \theta^*\nabla\Pi'\right), \\[2mm]
\rho' + \tau_\rho\Delta t\nabla\cdot\left(\rho^*\mathbf{u}'\right), \\[2mm]
\theta' + \tau_\theta\Delta t\mathbf{u}'\cdot\nabla\theta^*, \\[2mm]
\frac{1-\kappa}{\kappa}\frac{\Pi'}{\Pi^*} - \frac{\rho'}{\rho^*} - \frac{\theta'}{\theta^*},
\end{cases}
\tag{72}
$$

where $\tau_{u,\theta,\rho}$ are relaxation parameters. Applying the mixed finite-element discretisation presented above to these operators results in:

$$
M_2^\mu\widetilde{u}' - P_{2\theta}^{\Pi^*}\widetilde{\theta}' - G^{\theta^*}\widetilde{\Pi}' = -\mathcal{R}_{\mathbf{u}},
\tag{73}
$$

$$
M_3\widetilde{\rho}' + D\left(\widehat{\rho}^*\widetilde{u}'\right) = -\mathcal{R}_\rho,
\tag{74}
$$

$$
M_\theta\widetilde{\theta}' + P_{\theta 2}^{\theta^*}\widetilde{u}' = -\mathcal{R}_\theta,
\tag{75}
$$

$$
M_3^{\Pi^*}\widetilde{\Pi}' - M_3^{\rho^*}\widetilde{\rho}' - P_{3\theta}^*\widetilde{\theta}' = -\mathcal{R}_\Pi.
\tag{76}
$$

Note that at convergence of the iterative procedure primed quantities vanish and (68) is solved, which, given the definitions (78)-(81) below, is equivalent to solving (46)-(48) and (41). In these expressions M_2^μ is the operator formed by combining the $\mathbb{W}_2$ mass matrix with the operator arising from the Rayleigh damping:

$$
M_2^\mu \equiv M_2 + \Delta t M_\mu.
\tag{77}
$$

Additionally, a number of definitions have been used here. First, from (46)-(48) and (41) the residuals from the current estimate of the solution are defined as

$$
\mathcal{R}_{\mathbf{u}} \equiv \Delt\left(M_2\delta_t\widetilde{u} + M_\mu\overline{\widetilde{u}}^1 - \overline{R_{\mathbf{u}}}^\alpha\right),
\tag{78}
$$

$$
\mathcal{R}_\rho \equiv \Delta t\left(M_3\delta_t\widetilde{\rho} - R_\rho^F\right),
\tag{79}
$$

$$
\mathcal{R}_\theta \equiv \Delta t\left(M_\theta\delta_t\widetilde{\theta} - R_\theta^A\right),
\tag{80}
$$

and

$$
\mathcal{R}_\Pi \equiv \left\langle \widehat{\sigma}, \det\mathbf{J}\left[\left(\widehat{\Pi}^{(k)}\right)^{\frac{1-\kappa}{\kappa}} - \frac{R}{p_0}\widehat{\rho}^{(k)}\widehat{\theta}^{(k)}\right]\right\rangle,
\tag{81}
$$

---

do $n = 1, N$ (begin time-step loop)

    - Given the solution $\mathbf{x}^n \equiv \left(\widehat{\mathbf{u}}, \, \widehat{\rho}, \, \widehat{\theta}, \, \widehat{\Pi} \right)^n$, let the first

        estimate for $\mathbf{x}^{n+1} \equiv \left(\widehat{\mathbf{u}}, \, \widehat{\rho}, \, \widehat{\theta}, \, \widehat{\Pi} \right)^{n+1}$ be $\mathbf{x}^{(0)} = \mathbf{x}^n$

    - Set $\mathbf{x}^* \equiv (\rho^*, \, \theta^*, \, \Pi^*) = \left(\widehat{\rho}, \, \widehat{\theta}, \, \widehat{\Pi} \right)^n$ and compute

        the operators in (73)-(76) for $\mathcal{L}\left(\mathbf{x}^* \right)$

    - Compute the time-level n components of $(\mathcal{R}_{\mathbf{u}}, \, \mathcal{R}_{\rho}, \, \mathcal{R}_{\theta}, \, \mathcal{R}_{\Pi})$

    do $k = 1, K$ (Newton iteration)

        - Set the advecting wind $\widehat{\overline{\mathbf{u}}}^{1/2} \equiv \frac{1}{2} \left(\widehat{\mathbf{u}}^{(k-1)} + \widehat{\mathbf{u}}^n \right)$

        - Compute the advection terms $\mathcal{F}\left(\widehat{\rho}^n, \, \widehat{\overline{\mathbf{u}}}^{1/2} \right), \, \mathcal{A}\left(\widehat{\theta}^n, \, \widehat{\overline{\mathbf{u}}}^{1/2} \right)$

        - Compute the time-level $n+1$ components of $(\mathcal{R}_{\mathbf{u}}, \, \mathcal{R}_{\rho}, \, \mathcal{R}_{\theta}, \, \mathcal{R}_{\Pi})$

        - Solve (71) to obtain the increments $\mathbf{x}' \equiv \mathbf{x}^{(k)} - \mathbf{x}^{(k-1)}$

          and hence the updated estimate $\mathbf{x}^{(k)}$ for the time-level $n+1$ fields.

    end do

end do

Table 2. Outline of the iterative solution procedure used within a timestep.

where the time level $n + 1$ variables in the definitions (9) for δ_t and (10) for $\overline{}^{\alpha}$ have been replaced by the latest iterates, denoted by superscript (k). Second, various operators are defined as

$$D \equiv \tau_\rho \Delta t \left\langle \widehat{\sigma}, \widehat{\nabla} \cdot \widehat{\mathbf{v}} \right\rangle, \tag{82}$$

$$G^{\theta^*} \equiv \tau_u \Delta t \left\langle c_p \widehat{\theta}^* \widehat{\nabla}_{\mathsf{C}} \cdot \widehat{\mathbf{v}} + \widehat{\mathbf{v}} \cdot \widehat{\nabla}_{\mathsf{C}} \left(c_p \widehat{\theta}^* \right), \widehat{\sigma} \right\rangle$$
$$\qquad -\tau_u \Delta t \langle\!\langle [\![c_p \widehat{\theta}^* \widehat{\mathbf{v}}]\!], \{ \widehat{\sigma} \} \rangle\!\rangle, \tag{83}$$

$$P_{2\theta}^{\Pi^*} \equiv \tau_u \Delta t \left\langle c_p \widehat{w} \widehat{\nabla}_{\mathsf{C}} \cdot \widehat{\mathbf{v}}, \widehat{\Pi}^* \right\rangle$$
$$\qquad +\tau_u \Delta t \left\langle \widehat{\mathbf{v}} \cdot \widehat{\nabla}_{\mathsf{C}} \left(c_p \widehat{w} \right), \widehat{\Pi}^* \right\rangle$$
$$\qquad -\tau_u \Delta t \langle\!\langle [\![c_p \widehat{w} \widehat{\mathbf{v}}]\!], \{ \widehat{\Pi}^* \} \rangle\!\rangle, \tag{84}$$

$$M_3^{\rho^*} \equiv \left\langle \widehat{\sigma}, \frac{\widehat{\sigma}}{\widehat{\rho}^*} \det \mathbf{J} \right\rangle, \tag{85}$$

$$M_3^{\Pi^*} \equiv \frac{1 - \kappa}{\kappa} \left\langle \widehat{\sigma}, \frac{\widehat{\sigma}}{\widehat{\Pi}^*} \det \mathbf{J} \right\rangle, \tag{86}$$

$$P_{\theta 2}^{\theta^*} \equiv \tau_\theta \Delta t \langle\!\langle [\![\widehat{w} \widehat{\mathbf{v}}]\!], \{ \widehat{\theta}^* \} \rangle\!\rangle$$
$$\qquad -\tau_\theta \Delta t \left\langle \widehat{\nabla}_{\mathsf{C}} \cdot \left(\widehat{w} \widehat{\mathbf{v}} \right), \widehat{\theta}^* \right\rangle, \tag{87}$$

$$P_{3\theta}^* \equiv \left\langle \widehat{\sigma}, \frac{\widehat{w}}{\widehat{\theta}^*} \det \mathbf{J} \right\rangle. \tag{88}$$

The subscripted operators P_{ij} denote projections that map from $\mathbb{W}_j$ to $\mathbb{W}_i$ (see appendix E for the derivation of $P_{\theta 2}^{\theta^*}$); D is a divergence operator that maps from $\mathbb{W}_2$ to $\mathbb{W}_3$; and G^{θ^*} is a gradient operator that maps from $\mathbb{W}_3$ to $\mathbb{W}_2$.

The system of equations (73)-(76) is solved using an iterative Krylov method that is preconditioned by an approximate Schur complement of the equations for the pressure increment. The approximate Schur complement is formed by using lumped forms of the M_2^μ and M_θ mass matrices. The right-hand side terms are then updated using the latest estimates for the prognostic variables. This includes the FV transport terms through the updated advecting wind field, see Table 2 for details. This process is iterated a number of times. For all results presented here four iterations are used.

7. Computational examples

In the following the results are presented of model runs on standard Cartesian benchmarks of atmospheric dynamics, drawing on the suite considered in Melvin *et al.* (2010) for the vertical slice tests, with additional 3D tests. The boundary setup has doubly periodic

boundary conditions in the horizontal and zero flux on the top and bottom boundaries. The test parameters are summarised in Table 3. As noted, while in principle the finite element methodology affords flexibility on the polynomial order, here the focus will be on results in the lowest-order case. Additionally a number of simplifications and specifications are made:

- All tests are in a non-rotating frame such that $\mathbf{\Omega} \equiv 0$.

- There are no monotonicity constraints applied to the model.

- All meshes are uniform and orthogonal in the χ_1 and χ_2 directions, this results in a simplified form of the coordinate Jacobian $\mathbf{J}$, see Appendix D.

- The coordinate fields are obtained from

$$\chi_1 = (1 - \varepsilon_1)\chi_1^- + \varepsilon_1 \chi_1^+, \tag{89}$$

$$\chi_2 = (1 - \varepsilon_2)\chi_2^- + \varepsilon_2 \chi_2^+, \tag{90}$$

$$\chi_3 = (1 - \varepsilon_3)\chi_3^- (\chi_1, \chi_2) + \varepsilon_3 \chi_3^+, \tag{91}$$

  where $\left(\chi_1^-, \chi_1^+\right)$ and $\left(\chi_2^-, \chi_2^+\right)$ are the constant minimum and maximum values of χ_1 and χ_2 respectively. $\chi_3^- (\chi_1, \chi_2)$ is the orographic profile, χ_3^+ is the constant height of the domain top and ε_i, $i = 1, 2, 3$ is a parameter that takes values between zero and one.

- The semi-implicit scheme is centred in time so that $\alpha = 1/2$ and the relaxation parameters $\tau_{u,\rho,\theta} = 1/2$. Additionally, 4 iterations of the Newton loop are used.

- Following Wood *et al.* (2014) the reference profiles $\mathbf{x}^*$ are taken to be based upon the start of timestep fields $\mathbf{x}^* \equiv \mathbf{x}^n$, however in contrast to Wood *et al.* (2014) there is no further modification of the profiles (i.e. static adjustment applied to θ^* or recomputation of ρ^*).

- A quadratic reconstruction of the density is used for the mass flux $\widehat{\mathcal{F}}$ and a quadratic reconstruction of the gradient term in the advective update $\widehat{\mathcal{A}}$.

- Where applied, the Rayleigh damping profile takes the same form as used in Melvin *et al.* (2010), i.e.

$$\mu(z) = \begin{cases} 0, & z < z_B, \\ \overline{\mu}\sin^2\left[\frac{\pi}{2}\left(\frac{z - z_B}{z_T - z_B}\right)\right], & z \geq z_B, \end{cases} \tag{92}$$

  where z_B is the height at which the Rayleigh starts, z_T is the top of the model domain and the parameter $\overline{\mu}$ is specific to each test case.

For the Cartesian domain used in these examples the general coordinate χ used previously is replaced by the standard Cartesian coordinates $\mathbf{x}$ so that $(\chi_1, \chi_2, \chi_3) \equiv (x, y, z)$. In this section w is used to denote the vertical component of the velocity $\mathbf{u}$ (i.e. $w = D\chi_3/Dt = Dz/Dt$) as distinct from the test function for $\mathbb{W}_\theta$.

7.1. Nonhydrostatic gravity waves

First, the model is tested on the nonhydrostatic gravity wave test in Skamarock and Klemp (1994). In a two-dimensional domain, $(x, z) \in [-150, 150]\,\mathrm{km} \times [0, 10]\,\mathrm{km}$, a potential temperature perturbation of the form:

$$\theta' = \frac{\theta_0 \sin(\pi z/H)}{1 + [(x - x_c)/a]^2}, \tag{93}$$

Test	Δx (km)	Δz (m)	Δt (s)	Domain (km×km)	Background Initial State	T_{surf} (K)	U (ms^{-1})	C
NHGW	1	1000	12	300×10	$N = 0.01\text{s}^{-1}$	300	20	0.24
DC	$0.025 - 0.4$	$25 - 400$	$0.25 - 4$	51.2×6.4	Isentropic $\theta = T_{\text{surf}}$	300	0	≈ 0.4
HMW	2	250	20	240×50	Isothermal $T = T_{\text{surf}}$	250	20	0.2
NHMW	0.4	250	5	144×35	$N = 0.01\text{s}^{-1}$	300	10	0.125
SH	0.5	300	8	100×30	$N = 0.01\text{s}^{-1}$	288	10	0.16
3DBH	0.2	200	4	60×16	$N = 0.01\text{s}^{-1}$	293.15	10	0.2
3DRB	0.01	10	1.25	1×1.5	Isentropic $\theta = T_{\text{surf}}$	300	0	≈ 0.36

Table 3. Model parameters for each test. Identifiers: NHGW - NonHydrostatic Gravity Waves; DC - Density Current; HMW- Hydrostatic Mountain Waves; NHMW - NonHydrostatic Mountain Waves; SH - Schär Hill test; 3DBH - Three-dimensional Bell-shaped Hill; 3DRB - Three-dimensional Rising Bubble. The Courant number is given by $C \equiv U\Delta t/\Delta x$: for cases where $U = 0$, C has been calculated using the largest value of $\mathbf{u}'$. The acoustic Courant number (using a representative speed of sound $C_s = 343$ m/s) varies from 3 up to 40. For all cases the surface pressure (away from, or in the absence of, orography) is $p_{\text{surf}} = 1000$ hPa $\Rightarrow \pi_{\text{surf}} = 1$. For 3DBH and 3DRB, $\Delta y = \Delta x$ and the domain size in the y direction is respectively 40 km and 1 km.

421   with $\theta_0 = 0.01\,\text{K}$, $x_c = 0$, $a = 5\,\text{km}$, $H = 10\,\text{km}$, is superposed on a background atmosphere with constant buoyancy frequency

422    $N = 0.01\,\text{s}^{-1}$ and a horizontal wind $U = 20\,\text{m s}^{-1}$. The initial potential temperature perturbation spreads out in the form of gravity

waves (Figure 2). The final perturbation is in line with results in the literature, and in particular with Melvin *et al.* (2010).
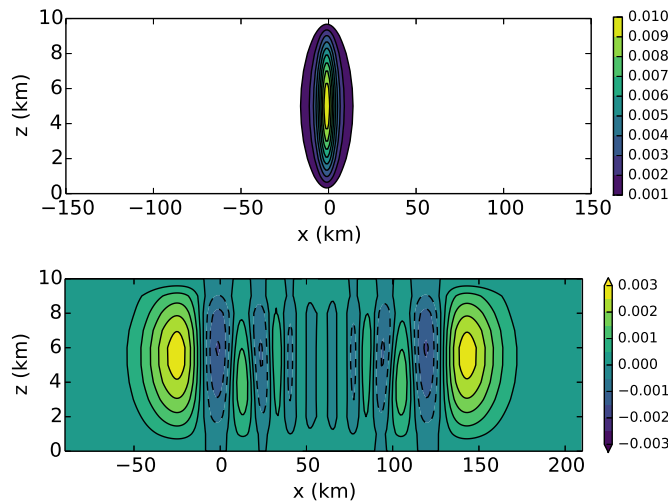

Figure 2. Potential temperature perturbation at the initial time (top panel, contours every 10^{-3} K) and at time $t = 3000\,\text{s}$ (bottom panel, contours every 5×10^{-4} K) for the nonhydrostatic inertia-gravity wave test.

423

424   *7.2.   Density current*

425   Next, the case of a falling cold air bubble in Straka *et al.* (1993) is considered. A negative thermal perturbation:

$$T' = \begin{cases} 0\ \text{K} & \text{if } r > 1 \\ -15\left[1 + \cos(\pi r)\right]/2\ \text{K} & \text{if } r < 1 \end{cases}, \tag{94}$$

426   where $r = \left\{[(x - x_c)/x_r]^2 + [(z - z_c)/z_r]^2\right\}^{0.5}$, $x_c = 0\,\text{km}$, $x_r = 4\,\text{km}$, $z_c = 3\,\text{km}$ and $z_r = 2\,\text{km}$,   is   superposed   on   a

427    $[-25.6, 25.6]\,\text{km} \times [0, 6.4]\,\text{km}$ motionless isentropic atmosphere with constant background $\theta = T_{\text{surf}} = 300\,\text{K}$. This test includes an

428   additional artificial diffusion term applied to the potential temperature and the components of the velocity vector of the form $\nu\nabla^2\phi$,

429   where ϕ is the prognostic variable, and $\nu = 75\,\text{m}^2\,\text{s}^{-1}$. Driven by its negative buoyancy, the bubble falls, hits the bottom boundary and

430   moves outward, developing vortices (Figure 3). Convergence with increasing resolution is evident from the final potential temperature

431   distribution. At the finest resolution and final time, the minimum perturbation value and the front location match the results in Melvin

432   *et al.* (2010) to within less than one percent (Table 4).

Grid size (m)	$\Delta\theta_{\min}$ (K)	$\Delta\theta_{\max}$ (K)	Front location (m)
400	-4.0704	0.5194	13939
200	-7.6091	0.1158	14941
100	-10.1768	0.1233	15313
50	-9.5342	0.0626	15384
25	-9.6589	0.0047	15402

Table 4. Minimum and maximum θ perturbation from the background state $\theta_{\mathrm{surf}} = 300\,\mathrm{K}$ and front location (rightmost intersection of $-1\,K$ contour with $z = 0$) in the density current test.
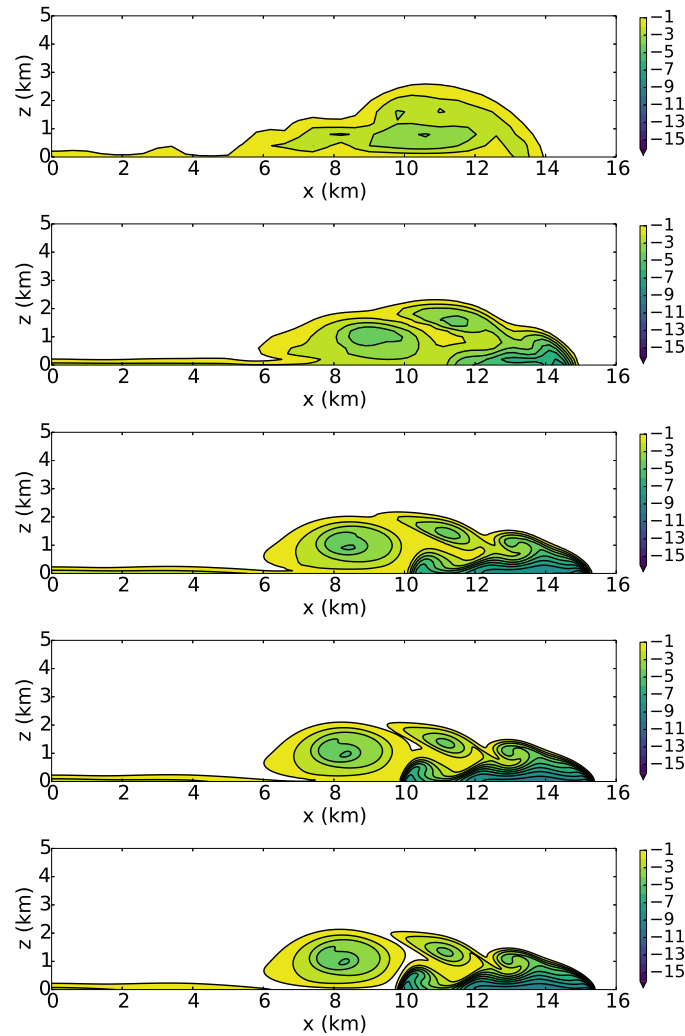
Figure 3. Potential temperature perturbation at time $t = 900\,\mathrm{s}$ for the density current test and resolutions (top to bottom panels) $\Delta x = 400, 200, 100, 50, 25\,\mathrm{m}$. Contours are plotted in the range $[-16, -1]$ K with a 1 K interval.

7.3. Linear hydrostatic/nonhydrostatic flow over a hill

The ability of the model to simulate orographically-driven flow is tested with idealised profiles of increasing slope. A height-based terrain-following coordinate (91) is used as in Melvin *et al.* (2010), and the thermodynamic variables are initially hydrostatically balanced.

In the first two tests, the bottom boundary is described by the function:

$$z_S = \frac{h_m}{1 + (x/a)^2}. \tag{95}$$

438   In particular, a hydrostatic flow is simulated by setting the height $h_m = 1$ m, half-width $a = 10$ km, and background wind speed

439    $U = 20$ m s^{-1}. The domain is a 240 km $\times$ 50 km isothermal atmosphere with background temperature $T = 250$ K. A damping layer is

440   used in the topmost 20 km of the domain, with $\overline{\mu}\Delta t = 0.3$, and final time $t = 15000$ s.

441   A nonhydrostatic flow is simulated using the same height h_m, a half-width $a = 1$ km, background wind speed $U = 10$ m s^{-1}, a

442   144 km $\times$ 35 km atmosphere with surface temperature $T_{\text{surf}} = 300$ K and constant buoyancy frequency $N = 0.01$ s^{-1}, a damping layer

443   in the topmost 10 km with $\overline{\mu}\Delta t = 0.15$, and final time $t = 9000$ s. In both the hydrostatic (Figure 4) and nonhydrostatic (Figure 5) flow

444   cases, the shape of the vertical velocity at final time of the mixed finite-element simulation compares favorably both with the results

445   from the semi-implicit-semi-Lagrangian model of Melvin *et al.* (2010) (referred to as ENDGame) and also the linear analytic solution

446   presented there.
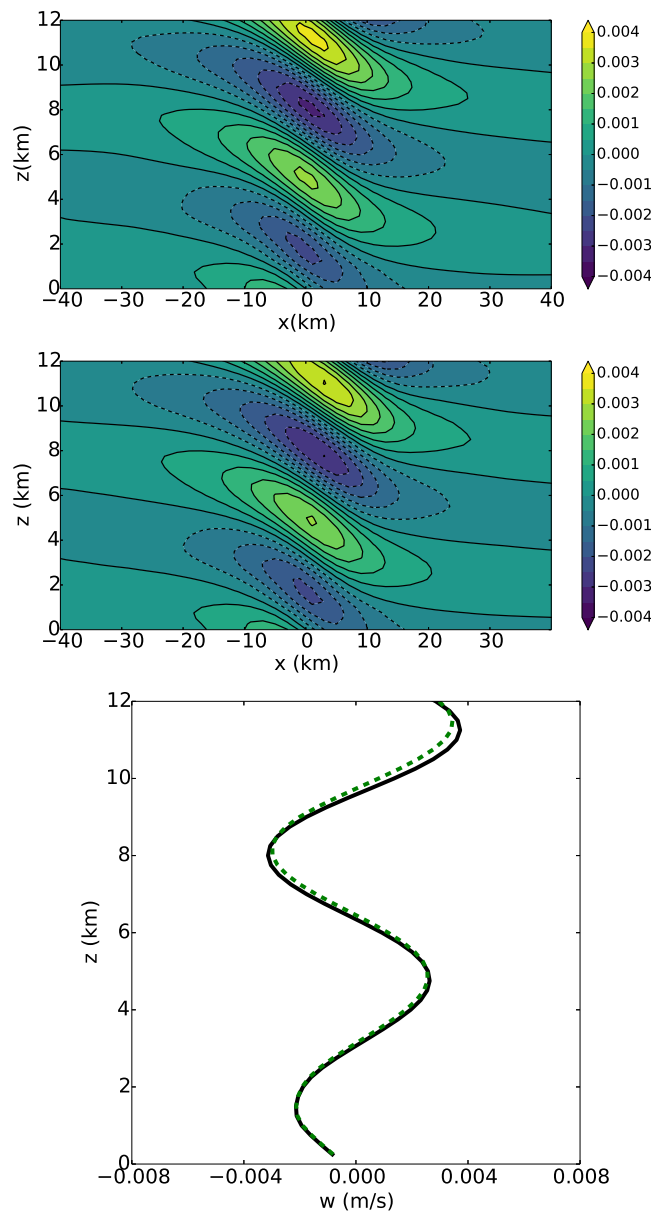
Figure 4. Vertical velocity perturbation w for the hydrostatic mountain wave test. Top panel: hydrostatic case result at time $t = 15000$ s, contours in the range $[-4, 4] \times 10^{-3}$ m s^{-1} with a 5×10^{-4} m s^{-1} interval. Middle panel: ENDGame, Melvin *et al.* (2010), Bottom panel: Profiles at $x = 0$ for the results from the current model (solid line) and from ENDGame (dashed line).
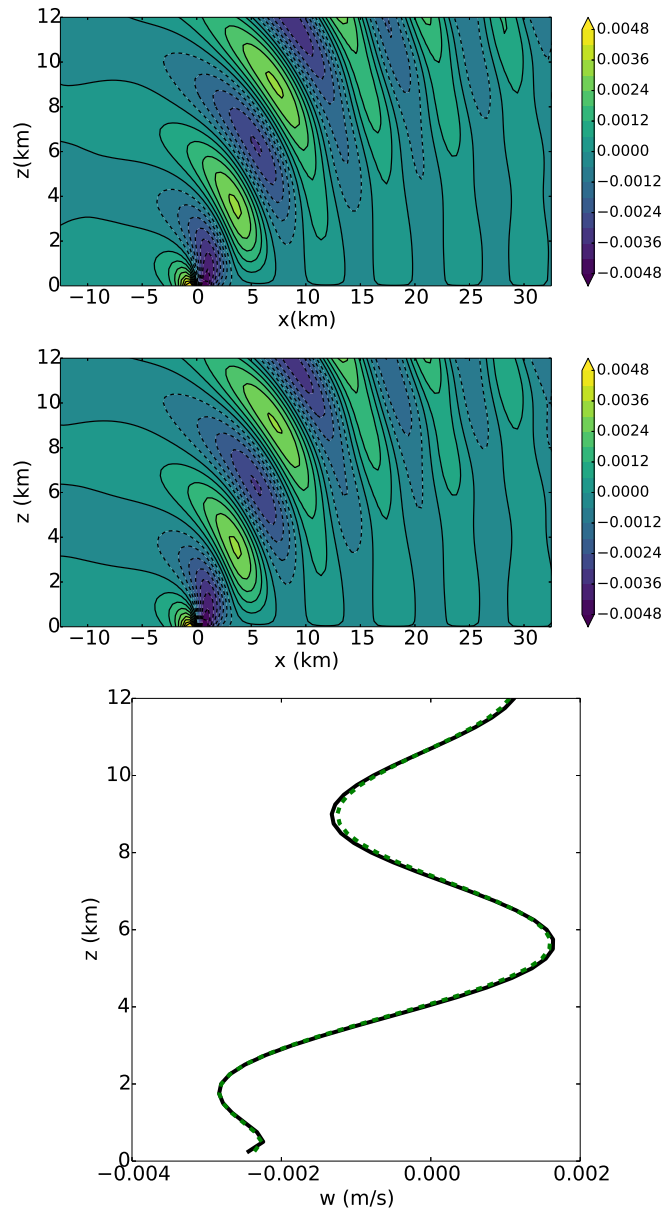
Figure 5. Vertical velocity perturbation w for the nonhydrostatic mountain wave test. Top panel: nonhydrostatic case result at time $t = 9000$ s, contours in the range $[-4.8, 4.8] \times 10^{-3}\,\mathrm{m\,s^{-1}}$ with a $6 \times 10^{-4}\,\mathrm{m\,s^{-1}}$ interval. Middle panel: ENDGame, Melvin *et al.* (2010), Bottom panel: Profiles at $x = 0$ for the results from the current model (solid line) and from ENDGame (dashed line).

447   *7.4. Schär hill*

448   In the third test a mountain range is considered with bottom boundary profile given by the function:

$$z_S = h_m \mathrm{e}^{-(x/a)^2} \cos^2\left(\frac{\pi x}{\lambda}\right), \tag{96}$$

449   with $h_m = 250$ m, $\lambda = 4$ km, and $a = 5$ km. The domain is a 100 km $\times$ 30 km atmosphere with surface temperature $T_{\mathrm{surf}} = 288$ K,

450   constant buoyancy frequency $N = 0.01\,\mathrm{s^{-1}}$, and a background wind $U = 10\mathrm{m\,s^{-1}}$. A damping layer is used in the top 10 km, with

451    $\overline{\mu}\Delta t = 1.2$. At final time $t = 2250$ s, the vertical velocity distribution matches the ENDGame result reasonably well (Figure 6), and

452   the amplitude of the waves above the mountain is again similar to both ENDGame and the results of Klemp *et al.* (2003). As with

453   ENDGame (Melvin *et al.* 2010) in order to obtain solutions that compare well with the linear solution a consistent discretisation of

454   certain metric terms is needed, as described in section 5.3.3. Without this correction the same distortion as seen in Klemp *et al.* (2003)

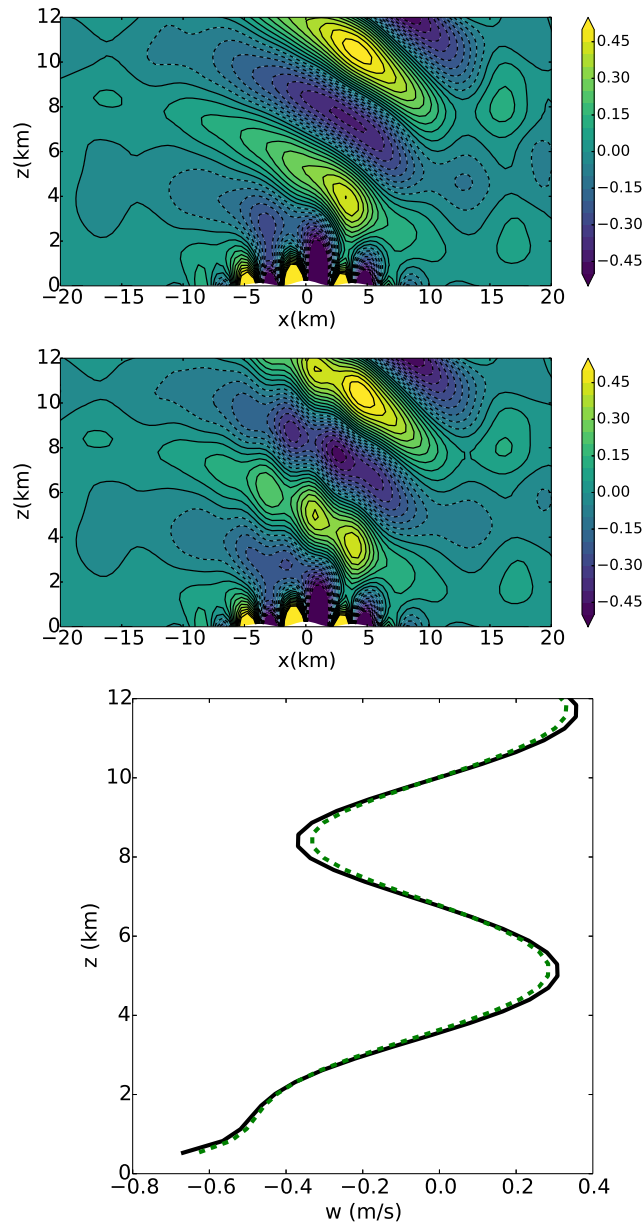455   and Melvin *et al.* (2010) of the waves above the mountain is present, (Figure 6, middle panel).

Figure 6. Vertical velocity perturbation w after 5 hours for the 2D Schär hill test. Contours are plotted in the range $[-0.5, 0.5]\,\mathrm{m\,s^{-1}}$ with a $5 \times 10^{-2}\,\mathrm{m\,s^{-1}}$ interval. Top panel: $\Delta t = 8\,\mathrm{s}$, middle panel: $\Delta t = 8\,\mathrm{s}$ with inconsistent metric terms, bottom panel: Profiles at $x = 0$ for the results with consistent metrics from the current model (solid line) and from ENDGame (dashed line) from Melvin *et al.* (2010).

456   *7.5.   3D medium-steep bell-shaped hill*

457   Next, the three-dimensional flow over a bell-shaped hill of Lock *et al.* (2012) and Yamazaki *et al.* (2016) is considered. The bottom

458   boundary profile is:

$$z_S = \frac{h_m}{[1 + (x/a)^2 + (y/a)^2]^{3/2}}, \tag{97}$$

459   with $h_m = 400\,\mathrm{m}$, $a = 1\,\mathrm{km}$. The maximum value of the derivative of (97) corresponds to an approximate slope of 20 degrees.

460   The domain is a $60\,\mathrm{km} \times 40\,\mathrm{km} \times 16\,\mathrm{km}$ atmosphere with surface temperature $T_{\mathrm{surf}} = 293.15\,\mathrm{K}$, constant buoyancy frequency $N =$

461    $0.01\,\mathrm{s^{-1}}$, and a background wind $U = 10\mathrm{m\,s^{-1}}$. A damping layer is used in the top $6\,\mathrm{km}$, with $\overline{\mu}\Delta t = 1.2$. The vertical velocity

462   distribution at final time $t = 3600\,\mathrm{s}$ is in line with the literature (Figure 7, cf. Figure 7 in Lock *et al.* (2012) and Figure 10 in Yamazaki
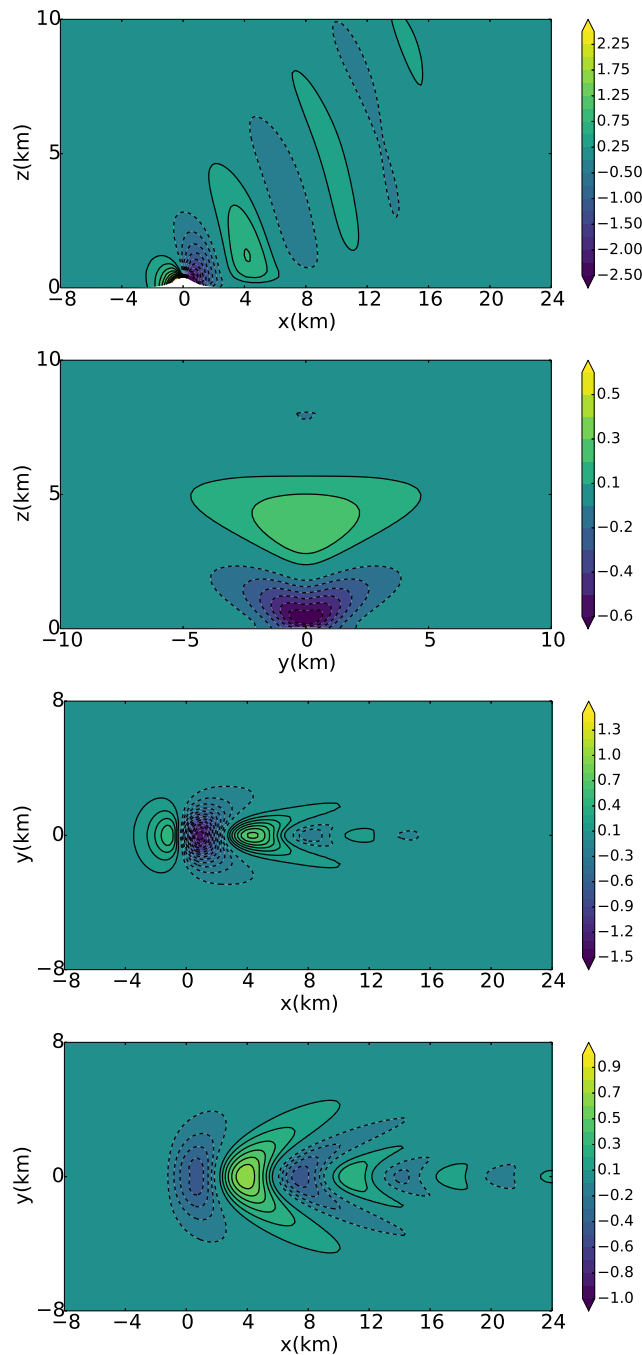
463   *et al.* (2016)).

Figure 7. Vertical velocity perturbation after 1 hour (900 time steps) for the bell-shaped hill test. Top to bottom panels: x-z slice at $y = 0$, y-z slice at $x = 2000$ m, x-y slice at $z = 800$ m, x-y slice at $z = 2000$ m,. The contour interval is $0.25 \, \mathrm{m \, s^{-1}}$ for the top panel, $0.1 \, \mathrm{m \, s^{-1}}$ otherwise.

464   *7.6.   3D rising bubble*

465   The 3D rising bubble test of Kelly and Giraldo (2012) is used. This simulates a buoyant thermal bubble on a neutrally stratified

466   isentropic background state with $\theta = T_{\mathrm{surf}} = 300 \, \mathrm{K}$ in a domain $1 \, \mathrm{km} \times 1 \, \mathrm{km} \times 1.5 \, \mathrm{km}$. A spherical perturbation of radius $r_0 = 250 \, \mathrm{m}$,

467   located at $(x_0, y_0, z_0) = (0, 0, 350)$ m is added to the background state. The perturbation is defined by

$$\theta' = \begin{cases} A \left[1 + \cos \left(\frac{\pi r}{r_0} \right) \right], & r \leq r_0, \\ \\ 0, & r > r_0, \end{cases} \tag{98}$$

468   with $r = \sqrt{\left[(x - x_0)^2 + (y - y_0)^2 + (z - z_0)^2 \right]}$ and $A = 0.25 \, \mathrm{K}$ as in Abdi and Giraldo (2016). Snapshots of the bubble at $t = 0$, 200

469   and $400 \, \mathrm{s}$ are shown in Figure 8 and a one-dimensional cross section at $x = y = 0$ in Figure 9. These results compare well with those

of Kelly and Giraldo (2012), notably maintaining a maximum value of the perturbation close to $0.5\,\text{K}$ and only exhibiting a small

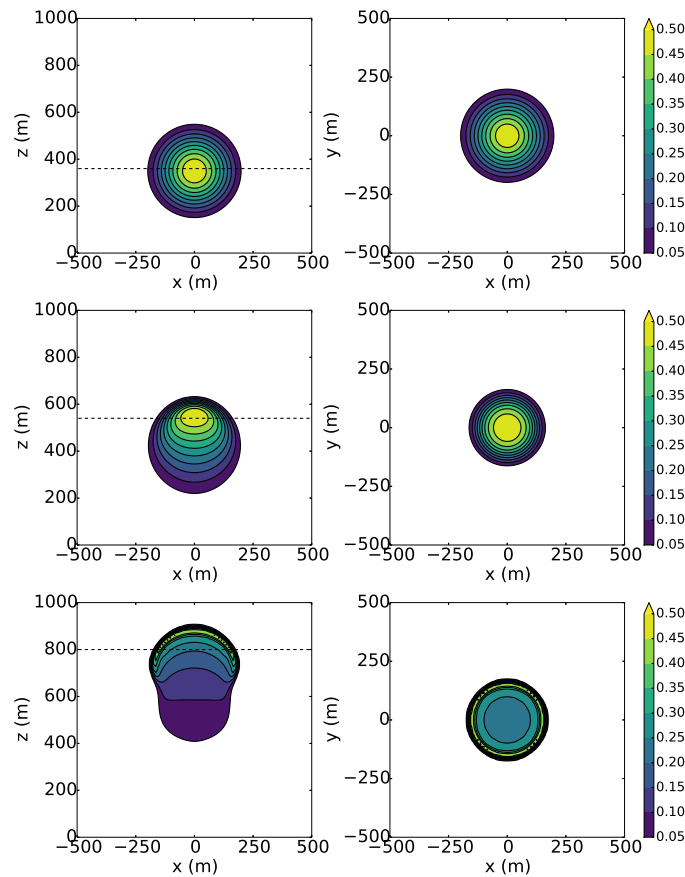undershoot above the bubble, comparable to the DG method of Kelly and Giraldo (2012).

Figure 8. Potential temperature perturbation from background state of $\theta = 300\,\text{K}$ for the 3D rising bubble test. Left column: $x - z$ slices at $y = 0$. Right column: $x - y$ slices taken at the level indicated by the dashed line in the $x - z$ slices. Top to bottom: initial data, $t = 200\,\text{s}$ and $t = 400\,\text{s}$ (all with contours in the range $[0.05, 0.5]\,\text{K}$ with a $0.05\,\text{K}$ interval).
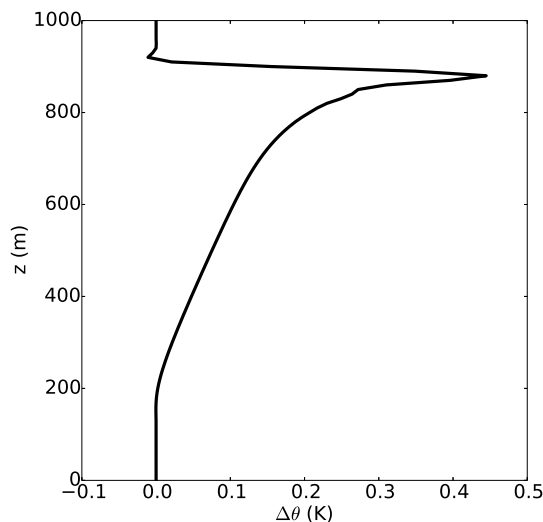
Figure 9. Potential temperature perturbation from background state of $\theta = 300\,\text{K}$ at $x = y = 0$ after $400\,\text{s}$ for the 3D rising bubble.

8. Summary

A method for coupling a mixed finite-element method alongside a finite-volume transport scheme and an iterative semi-implicit time

scheme has been presented. This method seeks to combine the benefits of all three schemes: the numerical consistency (independent

of the mesh) and accurate wave dispersion properties of the mixed finite-element scheme; the flexibility and accuracy of a high-order

Prepared using qjrms4.cls

upwind treatment of scalar advection from the finite-volume transport scheme; and the stable treatment of physically insignificant fast waves by the semi-implicit scheme.

The resulting model has been applied to a standard set of two-dimensional and three-dimensional test cases in Cartesian domains from the literature. This model has a similar level of accuracy to other models on these tests, including the semi-implicit-semi-Lagrangian ENDGame dynamical core currently used at the Met Office. Nevertheless, a range of improvements and extensions to the model presented here are currently being developed:

1. The discretisation presented here is valid for arbitrary quadrilateral based meshes and future work will report on the extension of this model to spherical three-dimensional domains using quasi-uniform grids.

2. The computation of the vorticity in the $\mathbb{W}_1$ space (19) used here can introduce spurious oscillations. Although this has minimal effect on the results shown here, upwind based schemes such as that used by Natale *et al.* (2016) are being investigated to improve on this aspect.

3. The method of lines scheme used to transport scalars imposes a timestep restriction on the model due to the CFL number constraint. Future work will investigate removing this constraint through using a flux-form semi-Lagrangian scheme for the scalars and possibly also for the velocity components.

Acknowledgments

A. Finite element spaces

Consider a domain D partitioned into a mesh consisting of D_C cells, D_F faces, D_E edges and D_V vertices. Denoting the coordinates by (χ_1, χ_2, χ_3) where χ_1 and χ_2 are horizontal coordinates and χ_3 a vertical coordinate, the finite element function spaces used here at order l for hexahedral elements correspond to:

$\mathbb{W}_0$ The Q_{l+1} space of scalar functions built from the tensor product of $P^{l+1}(\chi_1) P^{l+1}(\chi_2) P^{l+1}(\chi_3)$ polynomials of order $l+1$ with full continuity between cells. The dimension of this space is $\dim(\mathbb{W}_0) = D_V + l D_E + l^2 D_F + l^3 D_C$

$\mathbb{W}_1$ The Nédélec space of vector functions built from the tensor product of two P^{l+1} polynomials and one P^l polynomial with continuity between cells only in the tangential direction. The dimension of this space is $\dim(\mathbb{W}_1) = (l+1) D_E + 2l (l+1) D_F + 3l^2 (l+1) D_C$

$\mathbb{W}_2$ The Raviart-Thomas space of vector functions built from the tensor product of one P^{l+1} polynomial and two P^l polynomials with continuity between cells only in the normal direction. The dimension of this space is $\dim(\mathbb{W}_2) = (l+1)^2 D_F + 3l (l+1)^2 D_C$

$\mathbb{W}_3$ The Q_l^{DG} space of scalar functions built from the tensor product of $P^l(\chi_1) P^l(\chi_2) P^l(\chi_3)$ polynomials with no continuity between cells. The dimension of this space is $\dim(\mathbb{W}_3) = l^3 D_C$

510 $\mathbb{W}_\theta$ The space of scalar functions $P^l(\chi_1) P^l(\chi_2) P^{l+1}(\chi_3)$ based on the vertical part of $\mathbb{W}_2$. These are discontinuous between cells

511 in the horizontal directions but continuous between cells in the vertical direction. The dimension of this space is $\dim(\mathbb{W}_\theta) =$

512 $(l+1)^2 \mathsf{D_F^*} + l(l+1)^2 \mathsf{D_C}$ where $\mathsf{D_F^*}$ is a subset of $\mathsf{D_F}$ containing only the faces in the χ_3 direction

513 $\mathbb{W}_\chi$ The Q_m^{DG} space of scalar functions built from the tensor product of $P^m(\chi_1) P^m(\chi_2) P^m(\chi_3)$ polynomials with no continuity,

514 where m may be different from l. The dimension of this space is $\dim(\mathbb{W}_\chi) = m^3 \mathsf{D_C}$

B. Basis functions

516 For hexahedral elements each basis function can be decomposed into the tensor product of three orthogonal polynomials, multiplied

517 by a unit vector for the basis functions in the vector spaces $\mathbb{W}_1$ and $\mathbb{W}_2$. Two orders of polynomial functions are required in order to

518 fully specify the basis functions; if the functions in $\mathbb{W}_3$ are order l the two sets of polynomials can be denoted by

$$F_i(\eta) \equiv \prod_{\substack{j=0 \\ j \neq i}}^{l+1} \frac{\eta - \eta_j}{\eta_i - \eta_j}, \quad i = 0, \ldots, l+1, \tag{99}$$

519 and

$$G_i(\eta) \equiv \prod_{\substack{j=0 \\ j \neq i}}^{l} \frac{\eta - \eta_j}{\eta_i - \eta_j}, \quad i = 0, \ldots, l. \tag{100}$$

520 These are the Lagrange interpolating polynomials that take the value 0 at $\eta = \eta_j$, $j \neq i$, and the value 1 at $\eta = \eta_i$. Here η denotes a

521 generic coordinate. The polynomials F_i are of order $l+1$ and those for G_i are of order l. For $l = 0$ (100) is the empty product giving

522 $G_0(\eta) \equiv 1$. The locations of the basis nodal points η_j are evenly spaced in the computational coordinate η and include the endpoints,

523 $\eta = 0, 1$. For constant functions the centre point $\eta = 1/2$ is nominally used as the nodal point. Using (99) and (100) then the basis

524 functions, in the reference coordinates $\widehat{\chi} \equiv (\widehat{\chi}_1, \widehat{\chi}_2, \widehat{\chi}_3)$, for space $\mathbb{W}_0$ are given by

$$\gamma_{ijk}(\widehat{\chi}) \equiv F_i(\widehat{\chi}_1) F_j(\widehat{\chi}_2) F_k(\widehat{\chi}_3). \tag{101}$$

525 Those in $\mathbb{W}_1$ are given by

$$\mathbf{c}_{ijk}(\widehat{\chi}) \equiv \begin{cases} G_i(\widehat{\chi}_1) F_j(\widehat{\chi}_2) F_k(\widehat{\chi}_3) \mathbf{i}, \\ F_i(\widehat{\chi}_1) G_j(\widehat{\chi}_2) F_k(\widehat{\chi}_3) \mathbf{j}, \\ F_i(\widehat{\chi}_1) F_j(\widehat{\chi}_2) G_k(\widehat{\chi}_3) \mathbf{k}. \end{cases} \tag{102}$$

526 Those in $\mathbb{W}_2$ are given by

$$\mathbf{v}_{ijk}(\widehat{\chi}) \equiv \begin{cases} F_i(\widehat{\chi}_1) G_j(\widehat{\chi}_2) G_k(\widehat{\chi}_3) \mathbf{i}, \\ G_i(\widehat{\chi}_1) F_j(\widehat{\chi}_2) G_k(\widehat{\chi}_3) \mathbf{j}, \\ G_i(\widehat{\chi}_1) G_j(\widehat{\chi}_2) F_k(\widehat{\chi}_3) \mathbf{k}. \end{cases} \tag{103}$$

527 Those in $\mathbb{W}_\theta$ are given by

$$w_{ijk}(\widehat{\chi}) \equiv G_i(\widehat{\chi}_1) G_j(\widehat{\chi}_2) F_k(\widehat{\chi}_3). \tag{104}$$

528 Finally those in $\mathbb{W}_3$ are given by

$$\sigma_{ijk}(\widehat{\chi}) \equiv G_i(\widehat{\chi}_1) G_j(\widehat{\chi}_2) G_k(\widehat{\chi}_3). \tag{105}$$
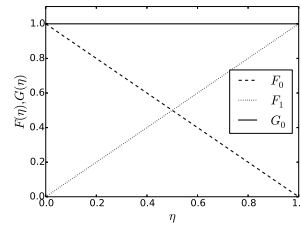
Figure 10. Basis functions needed for $l = 0$ order elements.

For the results presented here only the lowest-order elements, $l = 0$, are used. In this case, and assuming the basis nodal points for the linear functions F_i are at the extremities of the reference cell so that $\eta_0 = 0$ and $\eta_1 = 1$, (99) and (100) give:

$$F_0\left(\eta\right) = 1 - \eta, \tag{106}$$

$$F_1\left(\eta\right) = \eta, \tag{107}$$

and

$$G_0\left(\eta\right) = 1, \tag{108}$$

and these are shown in Figure 10.

C.   Evaluation of discontinuous fields at and across cell faces

Consider a function φ and an interior face F shared by cells C^- and C^+. Let $\mathbf{n}_{\mathsf{F}}^-$ be the vector normal to the face F that is outward pointing for cell C^- and let $\mathbf{n}_{\mathsf{F}}^+$ be the corresponding outward-pointing vector normal to face F for cell C^+. The inner and outer traces of φ on the face F are denoted by φ_{F}^- and φ_{F}^+, respectively. These are defined to be:

$$\varphi_{\mathsf{F}}^{\pm}(\mathbf{x}, t) \equiv \lim_{\varepsilon \to 0} \varphi(\mathbf{x} \pm \varepsilon \mathbf{n}_{\mathsf{F}}^-, t). \tag{109}$$

Then the face value of φ and the jump in φ across that face are defined, respectively, to be:

$$\{\varphi\}_{\mathsf{F}} \equiv \frac{1}{2}\left(\varphi_{\mathsf{F}}^+ + \varphi_{\mathsf{F}}^-\right), \tag{110}$$

and

$$[\![\varphi]\!]_{\mathsf{F}} = \varphi_{\mathsf{F}}^- \mathbf{n}_{\mathsf{F}}^- + \varphi_{\mathsf{F}}^+ \mathbf{n}_{\mathsf{F}}^+. \tag{111}$$

If the face F of cell C^- is an exterior face then define:

$$\{\varphi\}_{\mathsf{F}} = \varphi, \qquad [\![\varphi]\!]_{\mathsf{F}} = \varphi \mathbf{n}_{\mathsf{F}}^-. \tag{112}$$

If φ is a vector, then the multiplications in the definition of $[\![\varphi]\!]$ are dot products. Therefore, if φ is a scalar then $\{\varphi\}$ is also a scalar but $[\![\varphi]\!]$ is a vector, whilst if φ is a vector then $\{\varphi\}$ is also a vector but $[\![\varphi]\!]$ is a scalar.

543 **D. Evaluation of the Jacobian**

544 With a linear coordinate space the coordinates within a cell C are given by

$$
\begin{aligned}
\chi_i \;=\;& \chi_i^{(1)} F_0\left(\widehat{\chi_1}\right) F_0\left(\widehat{\chi_2}\right) F_0\left(\widehat{\chi_3}\right) \\
+\;& \chi_i^{(2)} F_1\left(\widehat{\chi_1}\right) F_0\left(\widehat{\chi_2}\right) F_0\left(\widehat{\chi_3}\right) \\
+\;& \chi_i^{(3)} F_0\left(\widehat{\chi_1}\right) F_1\left(\widehat{\chi_2}\right) F_0\left(\widehat{\chi_3}\right) \\
+\;& \chi_i^{(4)} F_1\left(\widehat{\chi_1}\right) F_1\left(\widehat{\chi_2}\right) F_0\left(\widehat{\chi_3}\right) \\
+\;& \chi_i^{(5)} F_0\left(\widehat{\chi_1}\right) F_0\left(\widehat{\chi_2}\right) F_1\left(\widehat{\chi_3}\right) \\
+\;& \chi_i^{(6)} F_1\left(\widehat{\chi_1}\right) F_0\left(\widehat{\chi_2}\right) F_1\left(\widehat{\chi_3}\right) \\
+\;& \chi_i^{(7)} F_0\left(\widehat{\chi_1}\right) F_1\left(\widehat{\chi_2}\right) F_1\left(\widehat{\chi_3}\right) \\
+\;& \chi_i^{(8)} F_1\left(\widehat{\chi_1}\right) F_1\left(\widehat{\chi_2}\right) F_1\left(\widehat{\chi_3}\right),
\end{aligned}
\tag{113}
$$

545 for $i = 1, \ldots, 3$. Here the mesh is further assumed to be uniform in the horizontal such that

$$
\chi_1^{(1)} \;=\; \chi_1^{(3)} = \chi_1^{(5)} = \chi_1^{(7)} = \chi_1^{-}, \tag{114}
$$

$$
\chi_1^{(2)} \;=\; \chi_1^{(4)} = \chi_1^{(6)} = \chi_1^{(8)} = \chi_1^{+}, \tag{115}
$$

$$
\chi_2^{(1)} \;=\; \chi_2^{(2)} = \chi_2^{(5)} = \chi_2^{(6)} = \chi_2^{-}, \tag{116}
$$

$$
\chi_2^{(3)} \;=\; \chi_2^{(4)} = \chi_2^{(7)} = \chi_2^{(8)} = \chi_2^{+}, \tag{117}
$$

546 and $\Delta\chi_1 \equiv \chi_1^{+} - \chi_1^{-}$ and $\Delta\chi_2 \equiv \chi_2^{+} - \chi_2^{-}$. Therefore the Jacobian can be simplified to

$$
\mathbf{J} =
\begin{bmatrix}
\Delta\chi_1 & 0 & 0 \\
0 & \Delta\chi_2 & 0 \\
\varepsilon_1 & \varepsilon_2 & \varepsilon_3
\end{bmatrix}
\tag{118}
$$

547 where ε_i denotes a linear interpolating function in the $\widehat{\chi_i}$ direction of the change in the χ_3 coordinate, i.e.

$$
\begin{aligned}
\varepsilon_1 \equiv{} & \left[\left(\chi_3^{(2)} - \chi_3^{(1)} \right) (1 - \widehat{\chi_2}) \right. \\
& + \left. \left(\chi_3^{(4)} - \chi_3^{(3)} \right) \widehat{\chi_2} \right] (1 - \widehat{\chi_3}) \\
& + \left[\left(\chi_3^{(6)} - \chi_3^{(5)} \right) (1 - \widehat{\chi_2}) \right. \\
& + \left. \left(\chi_3^{(8)} - \chi_3^{(7)} \right) \widehat{\chi_2} \right] \widehat{\chi_3},
\end{aligned}
\tag{119}
$$

$$
\begin{aligned}
\varepsilon_2 \equiv{} & \left[\left(\chi_3^{(3)} - \chi_3^{(1)} \right) (1 - \widehat{\chi_1}) \right. \\
& + \left. \left(\chi_3^{(4)} - \chi_3^{(2)} \right) \widehat{\chi_1} \right] (1 - \widehat{\chi_3}) \\
& + \left[\left(\chi_3^{(7)} - \chi_3^{(5)} \right) (1 - \widehat{\chi_1}) \right. \\
& + \left. \left(\chi_3^{(8)} - \chi_3^{(6)} \right) \widehat{\chi_1} \right] \widehat{\chi_3},
\end{aligned}
\tag{120}
$$

$$
\begin{aligned}
\varepsilon_3 \equiv{} & \left[\left(\chi_3^{(5)} - \chi_3^{(1)} \right) (1 - \widehat{\chi_1}) \right. \\
& + \left. \left(\chi_3^{(6)} - \chi_3^{(2)} \right) \widehat{\chi_1} \right] (1 - \widehat{\chi_2}) \\
& + \left[\left(\chi_3^{(7)} - \chi_3^{(3)} \right) (1 - \widehat{\chi_1}) \right. \\
& + \left. \left(\chi_3^{(8)} - \chi_3^{(4)} \right) \widehat{\chi_1} \right] \widehat{\chi_2}.
\end{aligned}
\tag{121}
$$

E. Finite-element advection of the reference potential temperature

549 The linear approximation $\mathcal{L}$ to the Jacobian $\mathcal{J}$ requires the evaluation of a finite-element estimate of the advection of the reference

550 potential temperature field θ^* by the increment to the wind, $\mathbf{u}'$, specifically $\langle w, \mathbf{u}' \cdot \nabla \theta^* \rangle$. However, since $\theta^* \in \mathbb{W}_\theta$ is horizontally

551 discontinuous, this term has to be integrated by parts. Following the same procedure as used to derive (18) together with the definitions

552 of appendix C, the result is:

$$
\begin{aligned}
\langle w, \mathbf{u}' \cdot \nabla \theta^* \rangle ={} & \sum_{\mathsf{C}} \langle w\mathbf{u}', \nabla \theta^* \rangle_{\mathsf{C}} \\
={} & \sum_{\mathsf{F}} \langle\!\langle [\![w\mathbf{u}']\!]_{\mathsf{F}}, \{ \theta^* \}_{\mathsf{F}} \rangle\!\rangle_{\mathsf{F}} \\
& - \sum_{\mathsf{C}} \langle \nabla_{\mathsf{C}} \cdot (w\mathbf{u}'), \theta^* \rangle_{\mathsf{C}} \\
={} & \langle\!\langle [\![w\mathbf{u}']\!], \{ \theta^* \} \rangle\!\rangle \\
& - \langle \nabla_{\mathsf{C}} \cdot (w\mathbf{u}'), \theta^* \rangle.
\end{aligned}
\tag{122}
$$

553 Transforming this expression to use the reference cell gives

$$
\begin{aligned}
\langle w, \mathbf{u}' \cdot \nabla \theta^* \rangle ={} & \langle\!\langle [\![\widehat{w}\widehat{\mathbf{u}}']\!], \left\{ \widehat{\theta^*} \right\} \rangle\!\rangle \\
& - \left\langle \widehat{\nabla}_{\mathsf{C}} \cdot (\widehat{w}\widehat{\mathbf{u}}'), \widehat{\theta^*} \right\rangle,
\end{aligned}
\tag{123}
$$

554 where $\langle\!\langle \cdot, \cdot \rangle\!\rangle$ now denotes the surface integrals over the collection of all cell faces evaluated using the reference cell and $[\![\cdot]\!]$ is defined in

555 terms of normal vectors defined for the reference cell. The form for $P_{\theta 2}^{\theta^*}$ given by (87) follows from this expression.

References

Abdi DS, Giraldo FX. 2016. Efficient construction of unified continuous and discontinuous Galerkin formulations for the 3d Euler equations. *Journal of Computational Physics* **320**: 46–68, doi:10.1016/j.jcp.2016.05.033.

Bochev PB, Ridzal D. 2010. Rehabilitation of the lowest-order Raviart-Thomas element on quadrilateral grids. *SIAM J. Num. Anal.* **47(1)**: 487–507.

Boffi D, Brezzi F, Fortin M. 2013. *Mixed finite element methods and applications*, *Computational Mathematics*, vol. 44. Springer: Berlin Heidelberg, doi:10.1007/978-3-642-36519-5.

Bott R, Raoul L. 1982. *Differential forms in algebraic topology*. Springer Press: New York, 1st edn.

Brezzi F, Fortin M. 1991. *Mixed and hybrid finite element methods*. Computational Mathematics, Springer: Berlin Heidelberg, doi:10.1007/978-1-4612-3172-1.

Cotter CJ, Shipton J. 2012. Mixed finite elements for numerical weather prediction. *J. Comput. Phys.* **231**: 7076–7091.

Cotter CJ, Thuburn J. 2014. A finite element exterior calculus framework for the rotating shallow-water equations. *J. Comp. Phys.* **257**: 1506–1526.

Gottlieb S. 2005. On high order strong stability preserving Runge-Kutta and multi step time discretizations. *J. Sci. Comput.* **25**: 105–128.

Guerra JE, Ullrich PA. 2016. A high-order staggered finite-element vertical discretization for non-hydrostatic atmospheric models. *Geoscientific Model Development* **9**(5): 2007–2029.

Kelly JF, Giraldo FX. 2012. Continuous and discontinuous Galerkin methods for a scalable three-dimensional nonhydrostatic atmospheric model: Limited-area mode. *Journal of Computational Physics* **231**(24): 7988–8008, doi:10.1016/j.jcp.2012.04.042.

Klemp JB, Skamarock WC, Fuhrer O. 2003. Numerical consistency of metric terms in terrain-following coordinates. *Mon. Wea. Rev.* **131**: 1229–1239.

Lauritzen P, Jablonowski C, Taylor M, Nair R (eds). 2011. *Numerical techniques for global atmospheric models*, *Lecture Notes in Computational Science and Engineering*, vol. 80. Springer, 1st edn.

Lawrence BN, Rezny M, Budich R, Bauer P, Behrens J, Carter M, Deconinck W, Ford R, Maynard C, Mullerworth S, Osuna C, Porter A, Serradell K, Valcke S, Wedi N, Wilson S. 2017. Crossing the chasm: How to develop weather and climate models for next generation computers? *Geoscientific Model Development Discussions* **11**: 1799–1821, doi:10.5194/gmd-2017-186, URL https://www.geosci-model-dev-discuss.net/gmd-2017-186/.

Lock SJ, Bitzer HW, Coals A, Gadian A, Mobbs S. 2012. Demonstration of a cut-cell representation of 3D orography for studies of atmospheric flows over very steep hills. *Mon. Wea. Rev.* **140**(2): 411–424, doi:10.1175/MWR-D-11-00069.1.

Melvin T, Benacchio T, Thuburn J, Cotter C. 2018. Choice of function spaces for thermodynamic variables in mixed finite element methods. *Q J R Meteorol. Soc.* **0**, doi:10.1002/qj.3268.

Melvin T, Dubal M, Wood N, Staniforth A, Zerroukat M. 2010. An inherently mass-conserving semi-implicit semi-Lagrangian discretisation of the nonhydrostatic vertical slice equations. *Q. J. R. Meteorol. Soc.* **136**: 799–814.

Monk P. 2003. *Finite element methods for Maxwell's equations*. Oxford University Press.

Natale A, Shipton J, Cotter CJ. 2016. Compatible finite element spaces for geophysical fluid dynamics. *Dynamics and Statistics of the Climate System* **1**(1), doi:10.1093/climsys/dzw005.

Rognes ME, Kirby RC, Logg A. 2009. Efficient assembly of H(div) and H(curl) conforming finite elements. *SIAM J. Sci. Comput.* **31**(6): 4130–4151.

Skamarock WC, Klemp JB. 1994. Efficiency and accuracy of the Klemp-Wilhelmson time-splitting technique. *Mon. Wea. Rev.* **122**: 2623–2630.

Staniforth A, Côté J. 1991. Semi-Lagrangian integration schemes for atmospheric models - a review. *Mon. Wea. Rev.* **119**: 2206–2223.

Staniforth A, Thuburn J. 2012. Horizontal grids for global weather prediction and climate models: a review. *Q. J. R. Meteorol. Soc.* **138**: 1–26.

Straka JM, Wilhelmson RB, Wicker LJ, Anderson JR, Droegemeier KK. 1993. Numerical solutions of a non-linear density current: A benchmark solution and comparisons. *Int. J. Num. Meth. Fluids* **17**: 1–22.

Thuburn J, Cotter CJ. 2015. A primal-dual mimetic finite element scheme for the rotating shallow water equations on polygonal spherical meshes. *Journal of Computational Physics* **290**(Supplement C): 274 – 297, doi:10.1016/j.jcp.2015.02.045.

Walters D, Boutle I, Brooks M, Melvin T, Stratton R, Vosper S, Wells H, Williams K, Wood N, Allen T, Bushell A, Copsey D, Earnshaw P, Edwards J, Gross M, Hardiman S, Harris C, Heming J, Klingaman N, Levine R, Manners J, Martin G, Milton S, Mittermaier M, Morcrette C, Riddick T, Roberts M, Sanchez C, Selwood P, Stirling A, Smith C, Suri D, Tennant W, Vidale PL, Wilkinson J, Willett M, Woolnough S, , Xavier P. 2017. The Met Office Unified Model Global Atmosphere 6.0/6.1 and JULES Global Land 6.0/6.1 configurations . *Geosci. Model Dev.* **10**: 1487–1520, doi:10.5194/gmd-10-1487-2017.

Williams KD, Harris CM, Bodas-Salcedo A, Camp J, Comer RE, Copsey D, Fereday D, Graham T, Hill R, Hinton T, Hyder P, Ineson S, Masato G, Milton SF, Roberts MJ, Rowell DP, Sanchez C, Shelly A, Sinha B, Walters DN, West A, Woollings T, Xavier PK. 2015. The Met Office Global Coupled model 2.0 (GC2) configuration. *Geoscientific Model Development* **8**(5): 1509–1524, doi:10.5194/gmd-8-1509-2015.

Wood N, Staniforth A, White A, Allen T, Diamantakis M, Gross M, Melvin T, Smith C, Vosper S, Zerroukat M, Thuburn J. 2014. An inherently mass-conserving semi-implicit semi-Lagrangian discretization of the deep-atmosphere global nonhydrostatic equations. *Q.J.R. Meteorol. Soc.* **140**: 1505–1520, doi:10.1002/qj.2235.

Yamazaki H, Satomura T, Nikiforakis N. 2016. Three-dimensional cut-cell modelling for high-resolution atmospheric simulations. *Q.J.R. Meteorol. Soc.* **142**(696): 1335–1350.